European Journal of Medicinal Chemistry 289 (2025) 117415

Contents lists available at ScienceDirect

European Journal of Medicinal Chemistry

journal homepage: www.elsevier.com/locate/ejmech

Research paper

Novel thiazolones for the simultaneous modulation of PPARγ, COX-2 and 15-LOX to address metabolic disease-associated portal inflammation

Mai S. El-Shoukrofy [a], Azza Ismail [a], Reem H. Elhamammy [b], Sherien A. Abdelhady [c], Rasha Nassra [d], Monica S. Makkar [e], Mahmoud A. Agami [e], Ahmed Wahid [b], Hisham A. Nematalla [f], Minh Sai [g], Daniel Merk [g,h], Ahmed F. El-Yazbi [e,i], Ahmed S.F. Belal [a], Ali H. Eid [j,*], Perihan A. Elzahhar [a,**]

[a] Department of Pharmaceutical Chemistry, Faculty of Pharmacy, Alexandria University, Alexandria, 21521, Egypt
[b] Department of Biochemistry, Faculty of Pharmacy, Alexandria University, Alexandria, 21521, Egypt
[c] Department of Pharmacology and Therapeutics, Faculty of Pharmacy, Pharos University in Alexandria, Canal El Mahmoudia Street, Beside Green Plaza Complex 21648, Alexandria, Egypt
[d] Department of Medical Biochemistry, Faculty of Medicine, Alexandria University, Alexandria, 21131, Egypt
[e] Faculty of Pharmacy and the Research & Innovation Hub, Alamein International University, Alamein, 5060335, Egypt
[f] Department of Pharmacology and Toxicology, Faculty of Pharmacy, Damanhour University, Damanhour, 22516, Egypt
[g] Department of Pharmacy, Ludwig-Maximilians-Universität München, 81377, Munich, Germany
[h] Institute of Pharmaceutical Chemistry, Goethe University Frankfurt, 60438, Frankfurt, Germany
[i] Department of Pharmacology and Toxicology, Faculty of Pharmacy, Alexandria University, Alexandria, 21521, Egypt
[j] Department of Basic Medical Sciences, College of Medicine, QU Health, Qatar University, Doha, 2713, Qatar

ARTICLE INFO

Keywords:
Thiazolones
PPARγ
COX-2
15-LOX
Multi-targeting
Liver inflammation
Metabolic diseases

ABSTRACT

A hybrid pharmacophore model, based on structural motifs previously identified by our team, was employed to generate ligands that simultaneously target COX-2, 15-LOX, and PPARγ in the context of metabolic dysfunction-associated fatty liver disease (MAFLD). Notable COX-2 inhibitory activities (IC_{50} = 0.065–0.24 μM) were observed relative to celecoxib (IC_{50} = 0.049 μM). The two most effective 15-LOX inhibitors, **2a** and **2b**, exhibited 69 % and 57 % of quercetin's action, respectively. Utilizing the rat hemi-diaphragm model to assess *in vitro* glucose uptake capacity, compounds **2a** and **2b** demonstrated significant glucose uptake potential in the absence of insulin, surpassing that of pioglitazone. Compound **2a** activated PPARγ with an EC_{50} value of 3.4 μM in a Gal4-hybrid reporter gene assay, indicating partial agonistic action. Interesting binding interactions with targets of interest were identified by molecular docking studies. As well, the expression levels of 20-HETE, Il-1β and TNF-α were decreased in LPS-challenged RAW264.7 macrophages upon treatment with compound **2a**. The pharmacokinetic analysis of **2a** and assessment of its *in vivo* efficacy in addressing hepatic impairment in rat models of diabetes and pre-diabetes were carried out. Together, these findings may offer preliminary insights into the potential of these compounds for further refinement in the existing therapeutic arsenals for metabolic diseases.

1. Introduction

Metabolic dysfunction-associated fatty liver disease (MAFLD) is a prevalent form of chronic liver disease that was formerly referred to as non-alcoholic fatty liver disease (NAFLD) [1,2]. It is associated with metabolic dysfunction indicators, including obesity and diabetes [1]. Hence, it is now regarded as the hepatic hallmark of the metabolic syndrome [3,4]. Persistent MAFLD can potentially advance to nonalcoholic steatohepatitis (NASH), liver fibrosis/cirrhosis, or even hepatocellular tumor [1,5,6]. The initial theoretical basis for the development of steatohepatitis was a "two-hit" theory, where the first strike involves the buildup of lipids in the liver, followed by a second hit featuring oxidative stress, necroinflammation and lipid peroxidation, which leads to the onset of NASH [7]. In this respect, portal inflammation is a typical finding in the majority of cases diagnosed with NASH and was recognized as an element of the inflammatory score in the

* Corresponding author.
** Corresponding author.
E-mail addresses: ali.eid@qu.edu.qa (A.H. Eid), perihan.elzahhar@alexu.edu.eg (P.A. Elzahhar).

https://doi.org/10.1016/j.ejmech.2025.117415
Received 22 December 2024; Received in revised form 12 February 2025; Accepted 16 February 2025
Available online 21 February 2025

MAFLD grading scheme developed by Brunt et al. [4,8]. Continuing research efforts focus on identifying new molecules capable of effectively treating MAFLD [1]. Resmetirom, an oral thyroid hormone receptor β agonist, is the sole therapeutic agent that received expedited FDA approval in March 2024 for the treatment of adults with non-cirrhotic NASH exhibiting moderate to advanced liver fibrosis, alongside lifestyle modifications related to diet and exercise [9].

In addition, farnesoid X receptor agonists, peroxisome proliferator-activated receptors (PPAR) agonists, C–C chemokine receptor type 2/5 antagonists, glucagon-like peptide-1 agonists and sodium-dependent glucose transporter 2 (SGLT2) inhibitors, are among the therapeutic classes under ongoing research to combat MAFLD [1,10,11].

Regarding PPARs, they belong to the ligand activated nuclear receptor super family. They are essential in controlling the transcription of genes involved in critical biological processes, including energy homeostasis and carbohydrate and lipid metabolism [12]. Notably, PPARγ, predominantly located in adipose tissue, serves a crucial role in adipocyte differentiation and adipogenesis. When activated, it enhances insulin sensitivity and reduces the flow of fatty acids to the liver [13]. Taking that into account, pioglitazone, a thiazolidinedione PPARγ agonist, has been shown to effectively reduce the amount of fat in the liver of patients with co-existing type 2 diabetes and NAFLD [1,12]. Besides, the combination of pioglitazone and vitamin E/vitamin E metabolites showed improvement in liver histology among diabetic patients with NASH [12,14,15]. Acknowledging the role of oxidative stress in the complex nature of NASH, it has been concluded that PPARγ reduced both inflammation and oxidative stress in NASH by regulating the miR-21–5p/SFRP5 pathway, resulting in a variety of therapeutic merits [16,17].

Since inflammation is one of the pillars of NASH pathophysiology, prior research documented COX-2 overexpression in chronic hepatitis and liver cirrhosis. Celecoxib (20 mg/kg/day) has been reported to reduce hepatic fibrosis in CCl4-and TAA-treated rats [18]. As well, markedly high COX-2 expression in MAFLD and NASH proposed its vital function in controlling the generation of downstream pro-inflammatory cytokines such as interleukin-1 (IL-1), IL-6, tumor necrosis factor-alpha (TNF-α) [19,20]. Over and above, 5-LOX and 12/15-LOX were shown to contribute to NAFLD and metabolic syndrome in humans. An analysis of plasma lipids in NASH showed a gradual rise in 5-LOX 5-HETE, and 12/15-LOX 15-HETE as MAFLD advanced to NASH [21].

Hence, it might be prudent to target the early inflammatory element that is characteristic of the metabolic dysfunction states that culminate in MAFLD. For this purpose, and based on our previous work [22,23], we opted to use a multi-target approach, involving PPARγ, COX-2, and 15-LOX, to interrupt the early inflammatory processes observed in prediabetes and type 2 diabetes [24,25]. In view of the foregoing, and in pursuit of our ventures in identifying multi-target directed ligands for intricate disorders, a molecular framework was constructed, relying on our previously reported leads. This would potentially target different lines of defense (COX-2, 15-LOX and PPARγ) of the metabolic disease especially portal inflammation. In the target compounds, we merged structural motifs from two lead structures discovered by our lab (Fig. 1). ***Lead structure 1*** [22] is a propargylic rhodanine derivative that was identified as a PPAR-γ partial agonist/selective COX-2 and 15-LOX inhibitor. ***Lead structure 2*** [23] is a thiazolone derivative substituted at position-2 with a cyclic secondary amine. It proved to be a dual COX-2/15-LOX inhibitor with appreciable *in vivo* anti-inflammatory activity. In this regard, the thiazolone ring represents the common scaffold from both leads that fused other units together. It formed an arylidene attachment with different propargylic aldehydes (as in ***lead structure 1***) and its 2-position is substituted with some cyclic secondary amines (as in ***lead structure 2***) to attain the final merged target compounds. Principally, our design conserved the three-module framework proposed by Pirat et al. featuring PPARγ agonist glitazones, which comprises a hydrophobic tail (propargyl group), an aromatic linker and a polar acidic head (thiazolone ring) [26]. Furthermore, the benzylidene linkage to the polar head was preserved in the designed compounds, which is likely responsible for the partial PPARγ agonistic activity that is believed to be free of the downsides that accompany full agonists [22]. Accordingly, we hereby describe the development, characterization and *in vivo* application of a new series of propargyl thiazolone derivatives, as COX-2 and 15-LOX inhibitors as well as PPARγ partial agonists. The anti-inflammatory and antioxidant potential in metabolic disease-associated portal inflammation was evaluated.

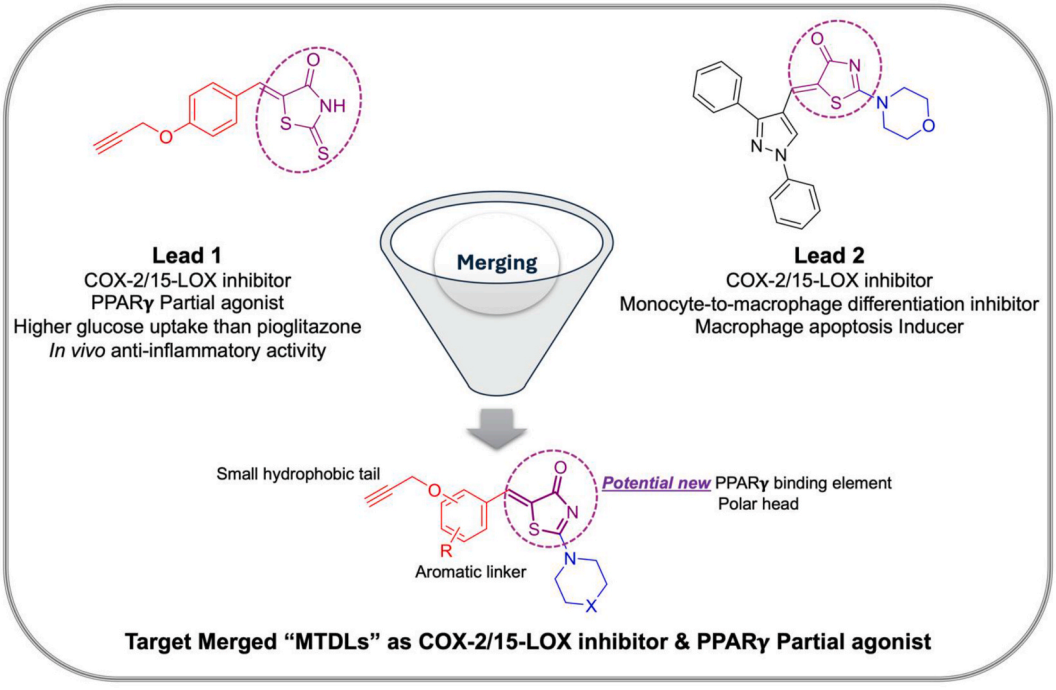

Fig. 1. Rationale for the design of the target compounds.

2. Results and discussion

2.1. Chemistry

The synthetic strategy adopted for the preparation of the target compounds (**2a-f**) and (**4a-f**) is outlined in Schemes 1 and 2. Three commercially available aldehydes namely; 4-hydoxybenzaldehyde, 4-hydroxy-3-methoxybenzaldehyde and 3-hydroxy-4-methoxybenzaldehyde were converted to their alkyne derivatives (**1a, b** and **3a, b**) by the reaction with propargyl bromide in acetone containing anhydrous K_2CO_3. The target compounds (**2a-f**) and (**4a-f**) were prepared via refluxing the aldehydes (**1a, b** and **3a, b**), rhodanine and cyclic secondary amines (namely; pyrrolidine, piperidine and morpholine) in ethanol containing catalytic amount of glacial acetic acid according to the reported one-pot reaction conditions [23]. During such one pot reaction, Knoevenagel condensation of the aldehyde and rhodanine was followed by substitution of the thioxo sulfur with the appropriate secondary amine that acts as both a catalyst (for Knoevenagel condensation) and also as a nucleophile in the substitution step.

2.2. Biological evaluation

2.2.1. In vitro COX-1/2 and 15-LOX inhibitory activities

The synthesized compounds (**2a-f** and **4a-f**) were tested to evaluate their *in vitro* COX-1/COX-2 inhibitory activities utilizing an ovine COX-1/human recombinant COX-2 assay kit. Concentrations suppressing 50 % of enzymatic activity (IC_{50}) were used to express the inhibitory activities of the tested compounds. Selectivity index (SI) values were also computed as IC_{50} (COX-1)/IC_{50} (COX-2). Indomethacin and diclofenac sodium, representing non-selective COX inhibitors, as well as the selective COX-2 inhibitor celecoxib, were used as positive controls for comparison. From the results reported in Table 1, it could be observed that all compounds exhibited enhanced COX-2 inhibitory activities when compared to diclofenac sodium and indomethacin, in addition to being more selective COX-2 inhibitors. In particular, compounds **2e** and **4a-e** showed two-digit nanomolar IC_{50} values comparable to that of celecoxib (65–97 nM versus 49 nM for celecoxib), while IC_{50} values of the other derivatives were in the low submicromolar range (0.10–0.24 μM).

Generally speaking, 3-substituted benzylidene derivatives **4a-f,** showed higher activity and selectivity as COX-2 inhibitors than the 4-substituted counterparts **2a-f**. The relatively lower SI values, even for the most active compounds such as **4a**, could be recognized as rewarding in the sense of avoiding cardiovascular side effects resulting from extensive COX-2 inhibition. Among series **2** compounds, the methoxy substituted derivatives **2e, f** (IC_{50} values 0.081 and 0.1 μM, respectively) were more active and selective as COX-2 inhibitors than their unsubstituted congeners **2b, c** (IC_{50} values 0.24 and 0.16 μM, respectively), while compounds **2a** and **2d** were almost equipotent. Moreover, compound **2e** (SI = 139) displayed ~60 % the COX-2 inhibition of celecoxib.

As for series **4** compounds, the pyrrolidine-containing compounds **4a** (SI = 234) and **4d** (SI = 173) exhibited superior COX-2 inhibition and selectivity when compared to **4b, c** and **4e, f**, respectively. They demonstrated 75 % and 64 % of the potency of celecoxib, respectively.

Next, we used a lipoxygenase inhibitor screening assay kit to test the capacity of the compounds as 15-lipoxygenase inhibitors (15-LOX) *in vitro*. The employed positive control was the 12/15-LOX inhibitor quercetin. Generally speaking, series **2** compounds were more potent than series **4**. In particular, compounds **2a-d** operated within the same order of magnitude as quercetin (IC_{50} 3.34 μM), and showed single-digit micromolar IC_{50} values (4.84–8.69 μM), which correspond to moderate to good 15-LOX inhibitory activity. The most active derivatives **2a** and **2b** possessed 69 and 57 % of the activity of quercetin, respectively.

The following SAR trends could be concluded; for COX-2 inhibition, series 2 compounds, bearing the benzylidene substitution in 4-position relative to the propargyloxy group, were generally less potent than their 3-sunbstituted congeners **4a-f**. Also given their comparatively lower COX-1 IC_{50} values, they showed lower selectivity indices. Among series 2 compounds, the piperidine and morpholine derivatives (**2e**, **2f**), which also featured an additional 3-methoxy substituent, showed more significant inhibition of COX-2 than their 3-unsubstituted counterparts (**2b**, **2c**).

Regarding series 4 compounds, derivatives lacking the methoxy group (**4a-c**) were more active than their 3-methoxy substituted homologues (**4d-f**). Roughly, and among the former compounds, COX-2 inhibitory activity was shown in the following order; pyrrolidine derivative **4a** > morpholine **4c** > piperidine **4b**. Whereas, among the later derivatives **4d-f**, the order was slightly different; pyrrolidine derivative **4d** > piperidine **4e** > morpholine **4f**.

As far as 15-LOX inhibition is concerned, and in contrast to COX-2 inhibition, series 2 compounds showed superior activity than series 4. More specifically, the 3-unsubstituted compounds **2a-c** exhibited more potent inhibition than the 3-methoxy substituted derivatives **2d-f**. In terms of the secondary amine substitution, the highest activity was demonstrated by the piperidine derivative **2b** followed by the pyrrolidine **2a** then the morpholine derivative **2c**.

2.2.2. In vitro glucose uptake assay

To examine the biological effects of these compounds as PPARγ-mediated insulin sensitizers, we assessed their capacity to stimulate glucose uptake both in the absence and presence of insulin. This was accomplished with the rat hemi-diaphragm method, as previously described [22]. The extent of glucose uptake was used as an indicator of their antidiabetic potential. We measured the change in glucose concentration in the working solution at the beginning and end of the experiment to determine the rate of glucose uptake by the rat hemi-diaphragm. The results were quantified as mg/g/45 min (Fig. 2). A thorough inspection of the glucose uptake trends shown by the test compounds indicated that **2f, 4a** and **4b** displayed comparable or slightly higher glucose uptake than pioglitazone without insulin, and noticeably higher uptake in its presence. Whereas compounds **2c**, **2d, 2e**, **4d** and **4e** were identified as insulin dependent glucose uptake

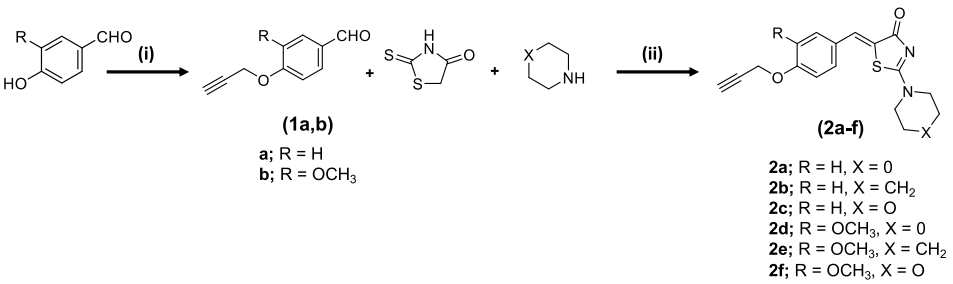

Scheme 1. Synthesis of the target compounds **2a-f**. Reagents and conditions: i) Propargyl bromide, K_2CO_3, Acetone, reflux for 2.5 h. ii) Ethanol, Acetic acid (cat.), reflux for 8–12 h.

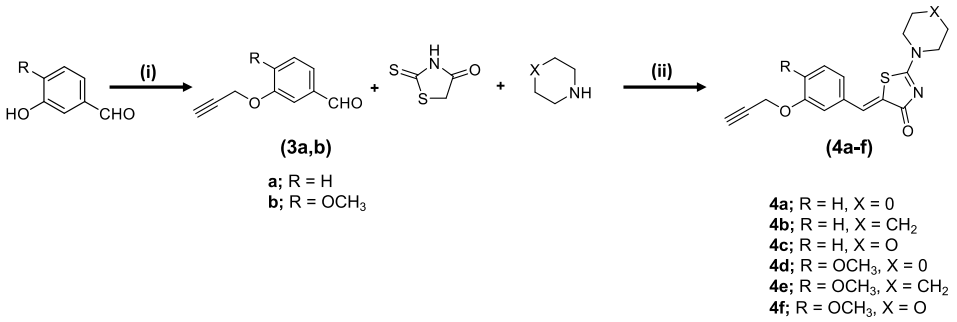

Scheme 2. Synthesis of the target compounds **4a-f**. Reagents and conditions: i) Propargyl bromide, K_2CO_3, Acetone, reflux for 2.5 h. ii) Ethanol, Acetic acid (cat.), reflux for 8–12 h.

enhancers as well but with slightly lower uptake than pioglitazone in absence of insulin and showing a comparable uptake to pioglitazone with insulin. Interestingly, compound **4f** demonstrated insulin independent glucose uptake capacity that was equivalent in magnitude to pioglitazone. Conversely, compounds **2a** and **2b** showed considerably higher glucose uptake activity without insulin, nonetheless, it displayed lower uptake with insulin indicative of a possible mixed agonist/antagonist response. Finally, compound **4c** did not exert any discernible variation from the negative control group.

2.2.3. KEGG (kyoto encyclopedia of genes and genomes) pathways enrichment analysis

In order to provide an *in silico* evidence to support the selection of PPARγ as potential target for the newly designed series, we carried out a target fishing study for the prototype compound **2a** using pharmmapper server. The latter returned PPARγ, among other targets (total 257), with Norm fit score of 0.5. Furthermore, Passonline tool predicted the bioactivities of compound **2a** as anti-inflammatory and in metabolic disease treatment. Then, all 257 targets were submitted to Venn tool to extract the targets that intersect or are shared with targets assigned to NAFLD or NASH (from disgenet database). This retrieved 8 common target genes namely; PPARD (peroxisome proliferator activated receptor delta), PPARA (peroxisome proliferator activated receptor alpha), JAK2 (Janus kinase 2), GSTM1 (glutathione S-transferase mu 1), NQO1 (NAD(P)H quinone dehydrogenase 1), PPARG (peroxisome proliferator activated receptor gamma), GSTP1 (glutathione S-transferase pi 1) and NR1H4 (nuclear receptor subfamily 1 group H member 4) (Fig. 3A). These genes were then subjected to KEGG pathway enrichment analysis (ShinyGO 0.80 tool) where the top 15 pathways were depicted in Fig. 3B. The enriched pathways which could be inherent to the study were PPAR signaling pathway (top enriched term), adipocytokine signaling pathway, hepatocellular carcinoma, non−alcoholic fatty liver disease, lipid and atherosclerosis, and reactive oxygen species, and the predicted protein-protein interaction network is also illustrated (Fig. 3C).

Results of the analysis consolidated the assumption that this new series has the ability to modulate PPARγ and other inflammatory targets, and chord with the associated signaling pathways in interplay as in Fig. 3C to serve in the mitigation of the underlying causes of metabolic disease-associated portal inflammation. Considering this, the PPAR family has been appreciated as a key controller in the development of NAFLD. For the most part, PPAR-γ influences its progression through insulin resistance, inflammation, lipid metabolism, oxidative stress, endoplasmic reticulum stress, and fibrosis [27].

2.2.4. PPARγ luciferase reporter assay

Compounds featuring different effects in the *in vitro* glucose uptake assay (**2a, 2b, 2e, 2f, 4a, 4b, 4e** and **4f**) were further profiled for PPARγ modulation in a Gal4-hybrid reporter gene assay. As shown in Table 2, compounds **2a** and **2e**, which had the *O*-propargyl group and the benzylidene-secondary amine moiety (pyrrolidine and piperidine) located in *para* positions to each other, activated PPARγ with EC_{50} values of 3.4 and 2.3 μM and moderate 18 % efficacy of pioglitazone, respectively. The inverted geometry in case of **4a** and **4b** resulted in slightly decreased PPARγ activation, nonetheless, they exerted 21 and 32 % of the activity of pioglitazone. Unfortunately, **2e, 4a** and **4b** proved to be toxic. Thus**, 2a** was selected for further biological testing.

2.2.5. Effect of compound 2a on the expression of inflammatory mediators

Several studies have shown a correlation between 15-LOX activity and cytokine production in different types of cells [23,28]. Interleukins (IL)-1β, 6, 12, and 15 are among the pro-inflammatory cytokines that have been demonstrated to be produced by macrophages as a result of 15-LOX activity and its metabolites [29]. As well, 20-hydroxyeicosatetraenoic acid (20-HETE) is produced as a general outcome of arachidonate metabolism [22]. Considering the above, we examined the effect of the most active compound **2a** on the expression levels of some inflammatory mediators in LPS-challenged RAW264.7 macrophages. As shown in Fig. 4, 48-h incubation with a non-cytotoxic concentration of the compounds (50 μg/ml) downregulated the expression levels of 20-HETE, IL-1β, and TNF-α by 36 %, 25 % and 34 % for **2a** and 54 %, 38 % and 24 % for celecoxib, respectively, relative to the untreated control.

2.2.6. Systemic and hepatic anti-inflammatory effects of compound 2a in rat models of metabolic impairment

The prototype compound **2a** was selected for *in vivo* assessment of its anti-inflammatory effect in two rat models of metabolic dysfunction. Prediabetes (Pre-D) and type 2 diabetes (D) were induced in Sprague-Dawley rats using protocols involving high-calorie feeding and high calorie feeding followed by streptozotocin (STZ), respectively, according to our previous work [24,25,30]. The anti-inflammatory effect of **2a** was compared to that of pioglitazone. The induction and treatment protocols are outlined in Fig. 5 below. Pre D and D rats received treatment with either pioglitazone or **2a** in the last two weeks of the protocol. Pioglitazone treated rats (Pre D Pio and D Pio) received 2 mg/kg/day of pioglitazone orally. This dose was shown in our previous work to produce a consistent anti-inflammatory effect in different tissues and organs in metabolically challenged rats without a concurrent hypoglycemic effect [24,25,31]. As for **2a**, an oral dose of 10 mg/kg/day was selected preliminarily on the premise of it being less than 1/20 of the predicted LD_{50} (350 mg/kg) [32] (https://tox.charite.de/protox3/#) [33]. In an initial study, the pharmacokinetic profile of a single oral administration of the selected dose was determined as described previously [34] (Fig. 6). The area under the curve (AUC), maximal serum concentration (C_{max}), and time for maximal serum concentration (T_{max}) were determined by non-linear regression and fitting to an AUC model using GraphPad Prism (version 7.00). Concurrently, the elimination rate constant (K_e) and half-life ($t_{1/2}$) were estimated from best fit values of the plasma concentration vs. time curve post-C_{max} using a one-phase decay model. The absorption rate constant (K_a) was computed from the single dose oral administration data using the method of residuals

Table 1
In vitro COX-1, COX-2, 15-LOX inhibitory IC_{50} values and COX SI values of the newly synthesized compounds.

Code	Structure	IC_{50} μM[a]			SI COX-1/COX-2[b]
		COX-1	COX-2	15-LOX	
Celecoxib		15.100	0.049	–	308
Diclofenac Na		5.100	0.840	–	6
Indomethacin		0.041	0.510	–	0.1
Quercetin		–	–	3.34	–
2a	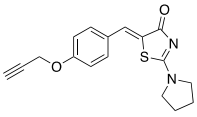	7.510	0.190	5.87	40
2b	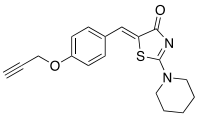	6.970	0.240	4.84	29
2c	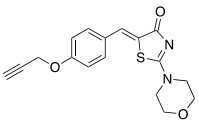	9.110	0.160	7.62	57
2d	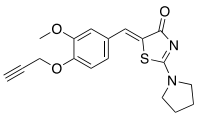	9.740	0.220	8.69	44
2e	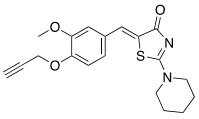	11.220	0.081	10.21	139
2f	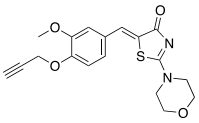	10.320	0.100	9.87	103
4a	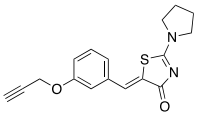	15.230	0.065	12.65	234
4b	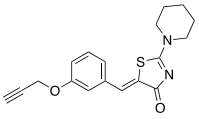	12.310	0.097	10.42	127
4c	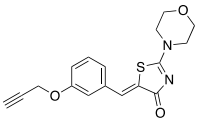	14.110	0.077	13.22	183
4d	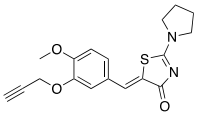	13.110	0.076	11.32	173
4e	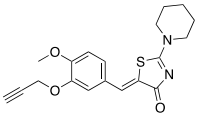	12.520	0.092	10.78	136

(*continued on next page*)

Table 1 (*continued*)

Code	Structure	IC_{50} μM[a]			SI COX-1/COX-2[b]
		COX-1	COX-2	15-LOX	
4f	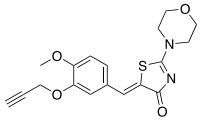	10.89	0.11	11.87	99

[a] IC_{50} is the concentration (μM) needed to cause 50 % inhibition of COX-1, COX-2 and 15-LOX enzymatic activity. All values are expressed as mean of three replicates with standard deviation less than 10 % of the mean.
[b] Selectivity index (SI)=IC_{50} (COX-1)/IC_{50} (COX-2).

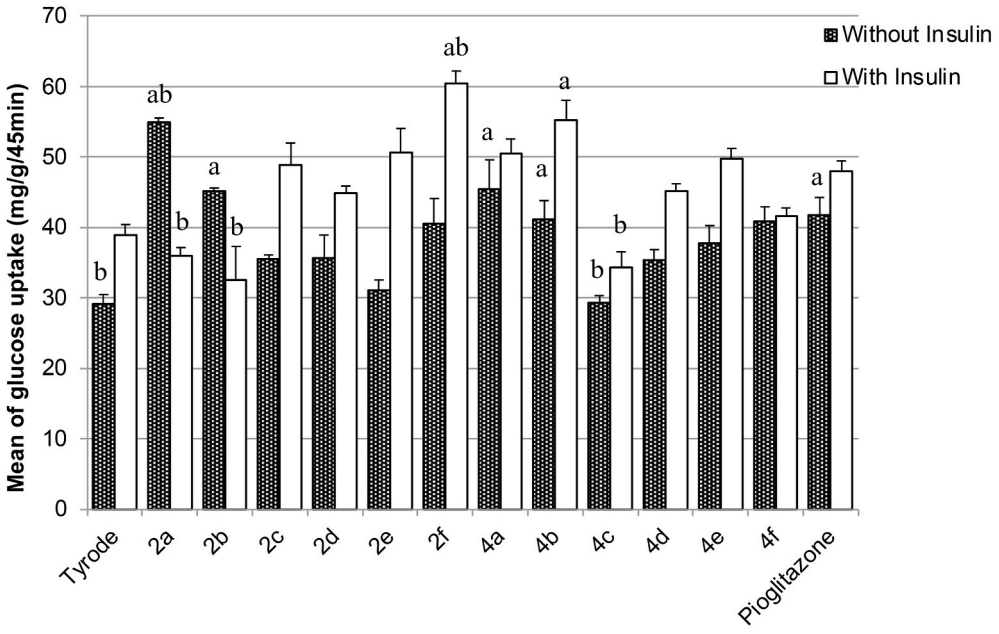

Fig. 2. *In vitro* glucose uptake activity of the test compounds both in absence and presence of insulin using rat hemi-diaphragm model. Data represented are mean ± SD of three replicates. Statistical analysis was performed using Two-way ANOVA followed by Sidak post hoc test. A P-value <0.05 was considered significant; a: statistically significant difference in comparison with Tyrode and b: statistically significant difference in comparison with pioglitazone.

[35]. These parameters were used to estimate the average serum concentration (C_{Av}) upon repeated daily oral administration, which was found to be within an ideal range to induce all the proposed biological effects as listed in Table 3. As such, this dose was selected for the treatment protocol to assess the *in vivo* anti-inflammatory activity.

In terms of body weight and fasting blood glucose levels, prediabetic rats did not differ from controls, while diabetic rats showed a decrease and an increase, respectively, as shown in our previous work [24,25,31]. These values were not further modified by either drug treatment (Fig. 7). Interestingly however, both drugs demonstrated a clear systemic anti-inflammatory effect whereby a reduction in serum proinflammatory cytokines and a restoration of total anti-oxidant capacity was observed following drug treatment in both Pre D and D rats (Fig. 8E–H). Indeed, increased hepatic and systemic oxidative stress and proinflammatory cytokines, particularly those assessed in the present study, were deemed a hallmark of these metabolically deranged rat models as observed in our prior investigation [24,25,31,36]. When assessed in liver tissue, drug treatment attenuated hepatic lipid peroxidation, which is a measure of oxidative stress, and inflammatory cytokine production in diabetic rats (Fig. 8A–D). These parameters were not observed to have equally large elevations in prediabetic rats under the present circumstances. The current observations strongly support an anti-inflammatory role for **2a** not only in hepatic tissue, but also systemically under conditions of metabolic impairment.

2.2.7. Molecular modeling and in silico predictions

2.2.7.1. Docking into COX-2 enzyme binding site. In pursuit of understanding the disclosed biological activity and acquiring a profound comprehension of the potential molecular interactions, docking simulations were conducted for compound **2a** within the active site of the COX-2 enzyme. The crystal structure of the latter (PDB ID: 1CX2) complexed with SC-558 (https://www.rcsb.org/structure/1cx2) served as an exemplar for inhibitory contacts using Molecular Operating Environment program (MOE 2019.0102). The most practical docking orientations were determined by applying both the MOE search method and scoring function. In addition, the binding affinity of the test compound towards the active site was assessed by considering energy scores, binding interactions with adjacent amino acids, and orientation in relation to the natural ligand. As a means to verify the implementation of the correct docking settings, the co-crystallized ligand was subjected to re-docking. The original PDB conformation was accurately replicated, as shown by a root mean square deviation (RMSD) of 0.81 Å and a docking score of −9.28 kcal/mol.

Probing of the binding mode of compound **2a** revealed a favorable anchoring within COX-2 active site (docking score −6.35 kcal/mol). It unveiled a hydrogen bond between the acceptor thiazolone carbonyl oxygen and Ser353. The generated complex was further stabilized through arene-hydrogen and arene-cation interactions between the phenyl ring with Tyr355 and Arg120, respectively (Fig. 9). **2a** also

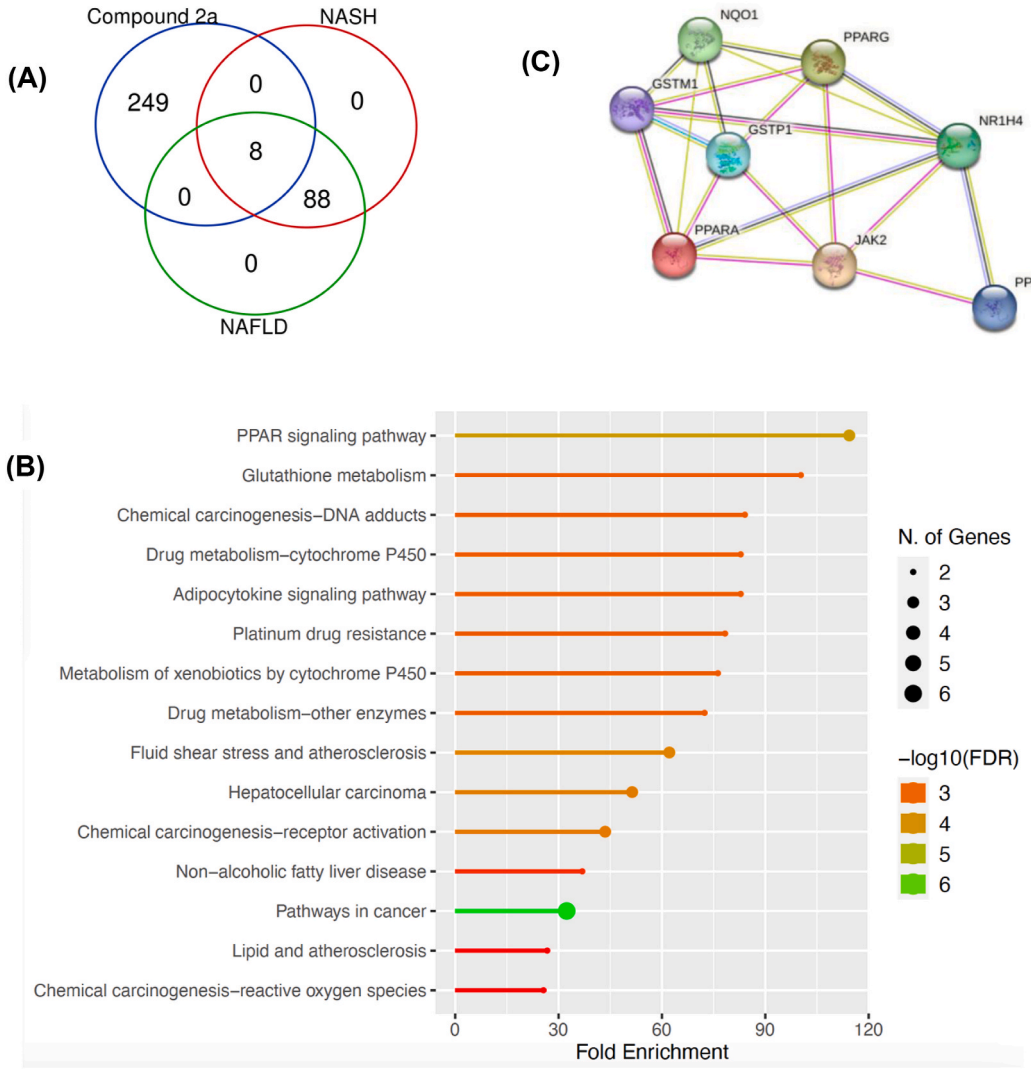

Fig. 3. KEGG pathways enrichment analysis. **(A)** Predicted targets of compound **2a** intersecting with those of NAFLD and NASH in a Venn diagram. **(B)** The top 15 enriched KEGG pathways of the 8 predicted common targets of compound **2a** with those of NAFLD and NASH. **(C)** The PPI network of the shared targets of compound **2a** targets with those of NAFLD and NASH as derived from Venn analysis.

Table 2
PPARγ-mediated transcriptional activity (EC_{50} values) of the most active compounds.

Code	PPARγ (EC_{50})[a]	Relative activity to the effect of 1 μM pioglitazone
2a	3.4 ± 2.2 μM	18 ± 2 % max. act.
2b	>30 μM	–
2e	2.3 ± 1.3 μM (toxic)	18 ± 3 % max. act.
2f	inactive at 30 μM	–
4a	5 ± 3 μM (toxic)	21 ± 2 % max. act.
4b	5 ± 3 μM (toxic)	32 ± 4 % max. act.
4e	>30 μM	–
4f	inactive at 10 μM and toxic at 30 μM	–

[a] Data represented are mean ± SD of at least three biological replicates.

aligned well with the co-crystallized ligand, extending over the same binding pocket.

2.2.7.2. Docking into 15-LOX enzyme binding site. The binding affinity of compound **2a** was estimated as well by docking into the crystal structure of 15-LOX enzyme (PDB ID: 1LOX) ((https://www.rcsb.org/structure/1LOX). This docking procedure was supported by the robust pose-retrieval of the co-crystallized ligand (RS7) on redocking into the appropriate binding region of 15-LOX, with an RMSD value of 0.59 Å and a docking score of −10.19 kcal/mol. Characterization of the most stable complex of compound **2a** exposed profitable fitting inside the enzyme's active site (docking score −7.57 kcal/mol), achieved by the formation of a hydrogen bond between the thiazolone sulfur atom and Leu597. Moreover, two arene-hydrogen interactions were located; one between the phenyl ring and Leu408, and another between the thiazolone ring and Gln548 (Fig. 10).

2.2.7.3. Docking into PPARγ ligand binding domain. The ligand binding domain (LBD) of PPARγ consists of 13 α-helices, labeled H1–H12 and H2′, as well as one β-sheet region [37]. The ligand binding pocket, situated in the core of the LBD, has three branches, each exhibiting distinctive features. Branch I, which includes H3, H5, H11, and H12, exhibits hydrophilic properties and serves as the location for ligand interaction with an acidic head group [37]. Branch II is hydrophobic and is encircled by H2', H3, H6, and H7, in addition to the *β*-sheet area. On the other hand, branch III, bordered by the *β*-sheet, H2, H3, and H5, contains both hydrophilic and hydrophobic parts. The activation function 2 (AF2) surface, composed of H12, H3, H4, and H5, is believed to be the site where full agonists stabilize via the triad Tyr473, His323, and

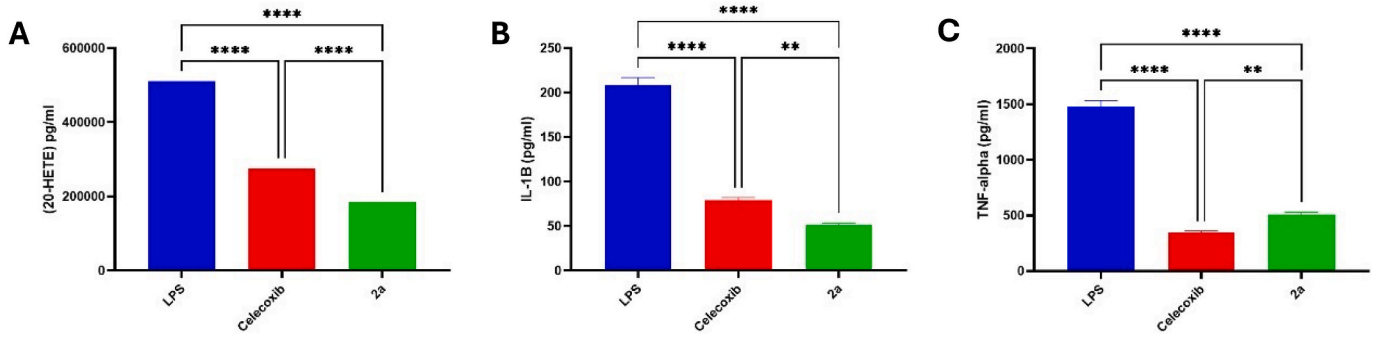

Fig. 4. Graphical representation of the expression levels of 20-HETE (**A**), IL-1β (**B**) and TNF-α (**C**), upon treatment of LPS-challenged RAW264.7 macrophages with compound **2a** and celecoxib. Results are presented as mean ± standard deviation of three separate replicas. Statistical analysis was carried out using One-way ANOVA followed by Tukey post hoc test. A P-value <0.05 was considered significant, **p < 0.01, and ****p < 0.0001.

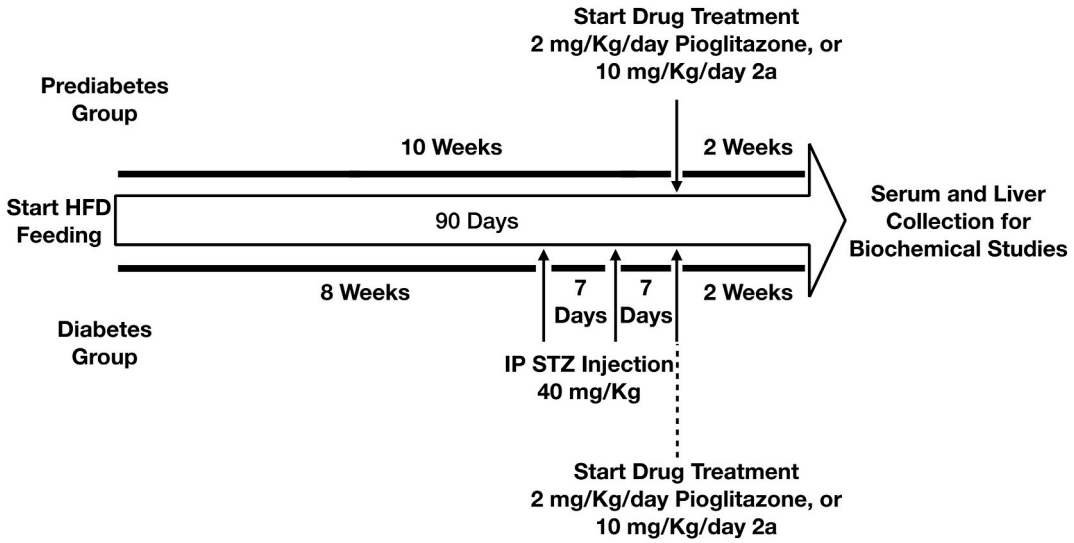

Fig. 5. A summary of the timeline for high-fat diet (HFD) feeding and treatment with streptozotocin (STZ) to generate the relevant rat models. The time points for drug treatment as well as the dosing are indicated on the timeline for the different groups.

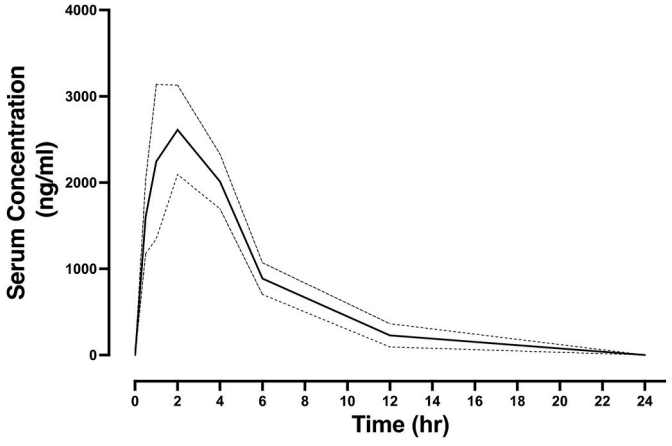

Fig. 6. The plasma concentration vs. time curves of **2a** after a single dose oral administration in Sprague-Dawley rats. The results shown are mean ± SEM of concentration values from five rats per group at 0, 0.5, 1, 2, 4, 8, 12, and 24 h post administration.

His449 of H12 [37]. Alternatively, it has been shown that partial agonists have a preference for selectively stabilizing certain parts of the LBD, particularly the *β*-sheet region [37].

Table 3
Measured and calculated pharmacokinetic parameters of compound **2a**.

Code	AUC (hr. ng/ml)	C_{max} (μM)	T_{max} (hr)	$t_{1/2}$ (hr)	K_e (hr^{-1})	K_a (hr^{-1})	C_{Av} (μM)
2a	16031	8.36	2	3.19	0.22	0.72	2.73

Therefore, docking simulations into PPARγ LBD were carried out to validate the *in vitro* partial agonistic activity exerted by compound **2a**. This was accomplished using the crystal structure of PPARγ LBD (PDB ID: 6E5A) (https://www.rcsb.org/structure/6e5a) in complex with our lead compound 1 (the partial agonist HV4). It was accurately placed upon redocking, with an RMSD of 1.3 Å and a docking score of −8 kcal/mol, confirming the reliability of the docking procedure used.

Investigation of the most energetically profitable pose of compound **2a** in the LBD of PPARγ revealed a typical binding pattern of partial agonists [37] (docking score −9.2 kcal/mol). It was optimally overlaid on the co-crystallized ligand sharing some interesting contacts (Fig. 11). For example, the thiazolone ring was engaged in arene-hydrogen interactions with Ser342 and Ile341, that are expected to stabilize the *β*-sheet region. Also, another hydrophobic interaction was established between the phenyl ring and Cys285 of H3.

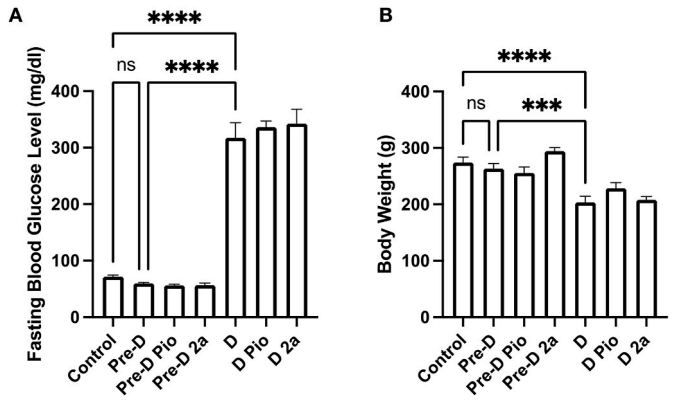

Fig. 7. Fasting blood glucose levels (A) and body weight (B) for rats in the different treatment groups. Pre-D and D denote prediabetic and type 2 diabetes rats, respectively. The results shown are mean ± SEM of values from five rats per group. Statistical significance was determined by one-way ANOVA followed by Tukey multiple comparisons test. $P < 0.05$ was considered significant and denoted by asterisks on the relevant comparisons.

2.2.7.4. In silico estimation of physicochemical properties, drug likeness, pharmacokinetic profile (ADMET) and ligand efficiency metrics. The structural analysis of orally delivered medications and drug candidates, as first proposed by Lipinski, has provided the foundational guidance necessary to associate physicochemical features with profitable drug development [38–41]. On top of that, Veber et al. proposed additional rules for oral bioavailability that depend on topological polar surface area and the number of rotatable bonds rather than molecular weight [42]. In this sense, the most active compound **2a** showed its conformity with the criteria of both rules (Table S1, Supplementary Material). Regarding pharmacokinetic characteristics, compound **2a** exhibited moderate cell permeability in the Caco-2 cell model (Tables S2 and S3, Supplementary Material). It demonstrated high human intestinal absorption and strong binding to plasma proteins. Moreover, it showed limited blood-brain barrier penetration capacity. Notably, it had a favorable toxicological profile with a predicted LD_{50} value of 350 mg/kg and a predicted toxicity class of 4. Meanwhile, increased molecular weight and lipophilicity have been shown to boost binding potency; however, they are also strongly associated with heightened binding promiscuity and reduced safety levels [43]. Efforts to integrate physicochemical parameters with potency into a quantitative model have culminated in the development of ligand efficiency indices. These are composite and straightforward indicators designed to enhance the effectiveness of the drug development process and yield superior outcomes [44].

Consequently, evaluation of the attributes of compound **2a** as a possible hit/lead was conducted using these indices: Ligand Efficiency (LE), Lipophilic Ligand Efficiency (LLE), and Ligand Efficiency-Dependent Lipophilicity Index (LELP) (Table S4, Supplementary

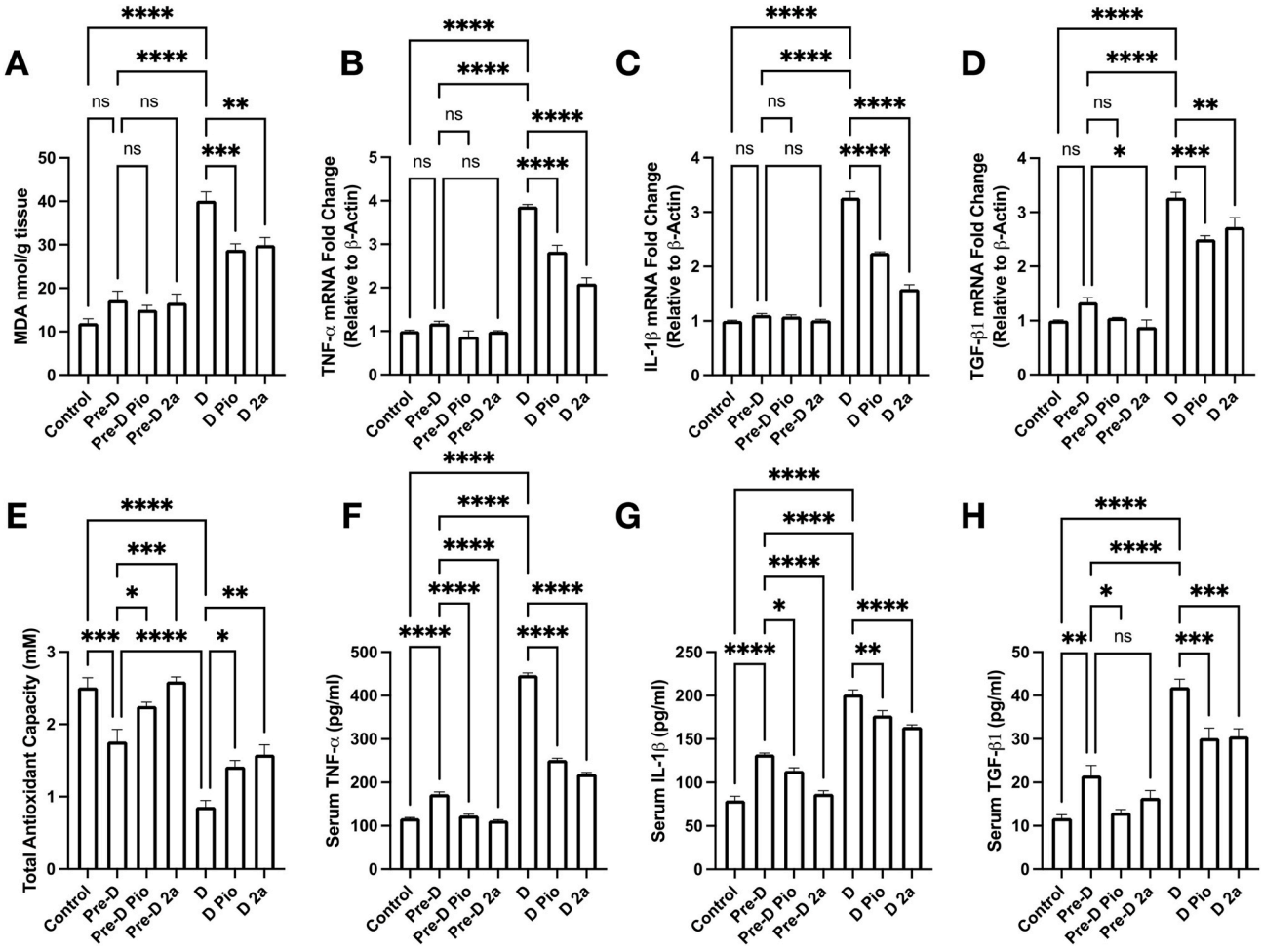

Fig. 8. Hepatic malondialdehyde and pro-inflammatory cytokine RNA levels (A–D), and total antioxidant capacity and serum pro-inflammatory cytokines and (E–H) for rats in the different treatment groups. Pre-D and D denote prediabetic and type 2 diabetes rats, respectively. The results shown are mean ± SEM of values from four rats per group. Statistical significance was determined by one-way ANOVA followed by Tukey multiple comparisons test. $P < 0.05$ was considered significant and denoted by asterisks on the relevant comparisons.

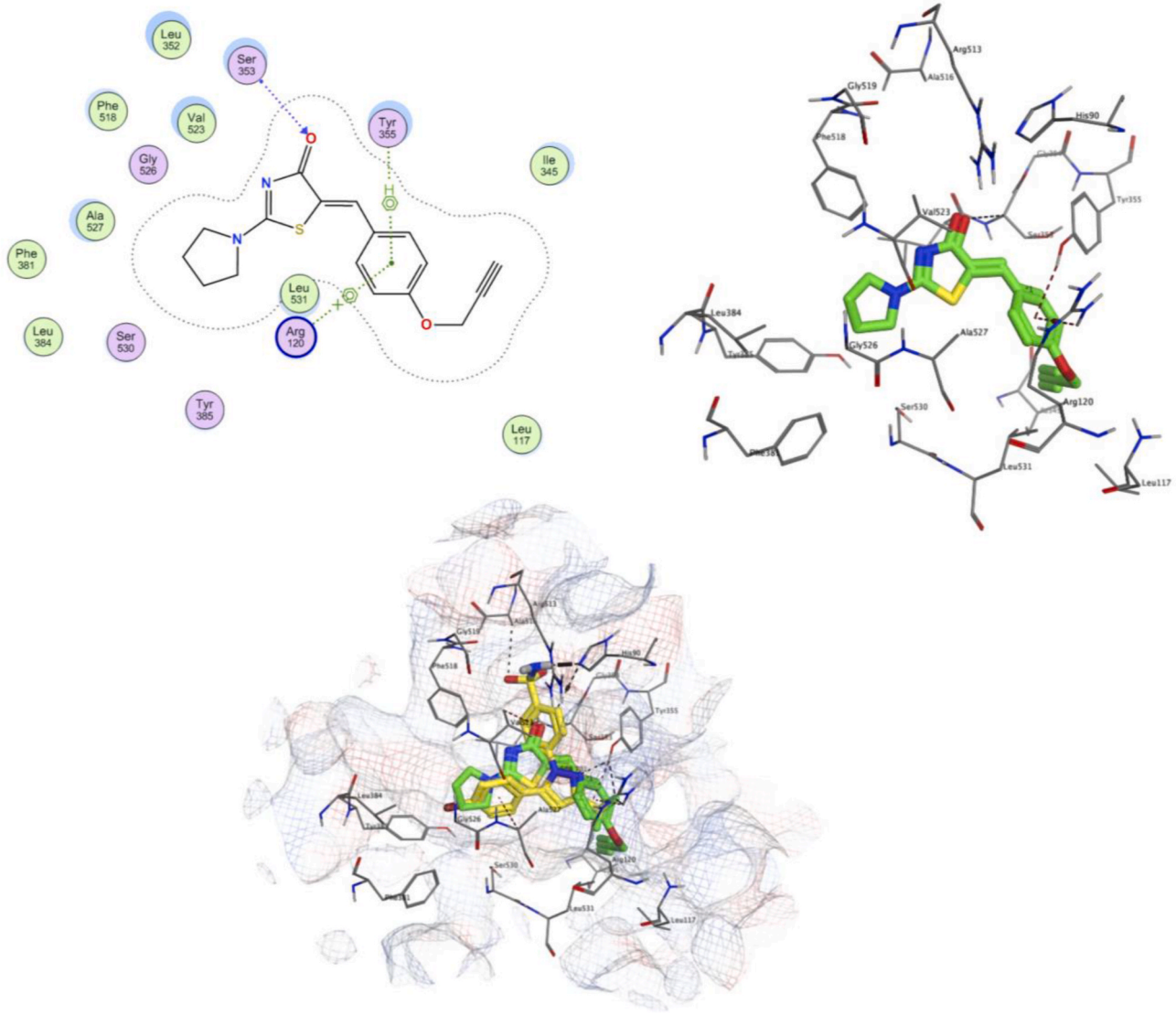

Fig. 9. Docking and binding pattern of compound **2a** inside the active site of COX-2 (PDB ID: 1CX2) as follows: The best docked pose in 2D (left upper panel), 3D (right upper panel) and overlaid on the native ligand SC-558 on a molecular surface (lower panel).

Material). LE serves as a connection between drug efficacy and molecular size, quantified by the number of heavy (non-hydrogen) atoms. Concerning the inhibitory actions of COX-2 and 15-LOX, the LE values were 0.43 and 0.33, respectively, which match the established minimum LE for lead compounds (about 0.3) or above 0.3 for drug candidates [45, 46]. LLE sets a relationship between potency and lipophilicity. The anti-COX2 activity of compound **2a** adhered to the optimal cut-off value for lead compounds ($\geq$3) [46], whereas its anti-LOX activity showed a slight deviation. LELP is a hybrid scoring function with a greater predictive ability because it couples molecular size and lipophilicity to potency. Aside from its strong association with pharmacokinetic profile and safety, LELP has the further benefit of being able to distinguish between approved drugs and failed leads, in contrast to LE and LLE [43]. It is worth noting that the inhibition of both COX and LOX by compound **2a** resulted in LELP values of 7.1 and 9.3, respectively, which met the approved limits for leads ($\leq$7.5) or marketed drugs (<10) [46]. In accordance with the estimated ligand efficiency, drug likeness, and pharmacokinetic parameters, compound **2a** proved its suitability for further lead optimization rounds.

3. Conclusions

Liver (portal) inflammation is recognized as a fundamental characteristic in the pathophysiology of MAFLD, which can potentially transition to NASH. The latter is a common factor in the constellation of metabolic-impairment based diseases, referred to as the metabolic syndrome. Such multifaceted disorder could benefit from combating portal inflammation at an early stage. In this context, a new series of propargylated thiazolone compounds was designed and synthesized to establish a multi-target matrix capable of simultaneously targeting multiple lines of defense of systemic and hepatic inflammation, in particular. Such matrix comprised the necessary pharmacophores for the intended targets; COX-2, 15-LOX and PPARγ, building on our previously reported lead compounds. This series was evaluated for its anti-inflammatory potential and demonstrated promising COX-2 inhibitory activities (0.065–0.24 μM) in comparison to celecoxib (0.049 μM). Additionally, inhibition of 15-LOX was observed, with the most potent derivatives **2a** and **2b** exhibiting 69 % and 57 % of quercetin's activity, respectively. All compounds were tested for their *in vitro* glucose uptake capability using rat hemi-diaphragm model in which different glucose uptake patterns were exhibited. Compounds **2a** and **2b** showed appreciable glucose uptake activity in the absence of insulin, even higher than

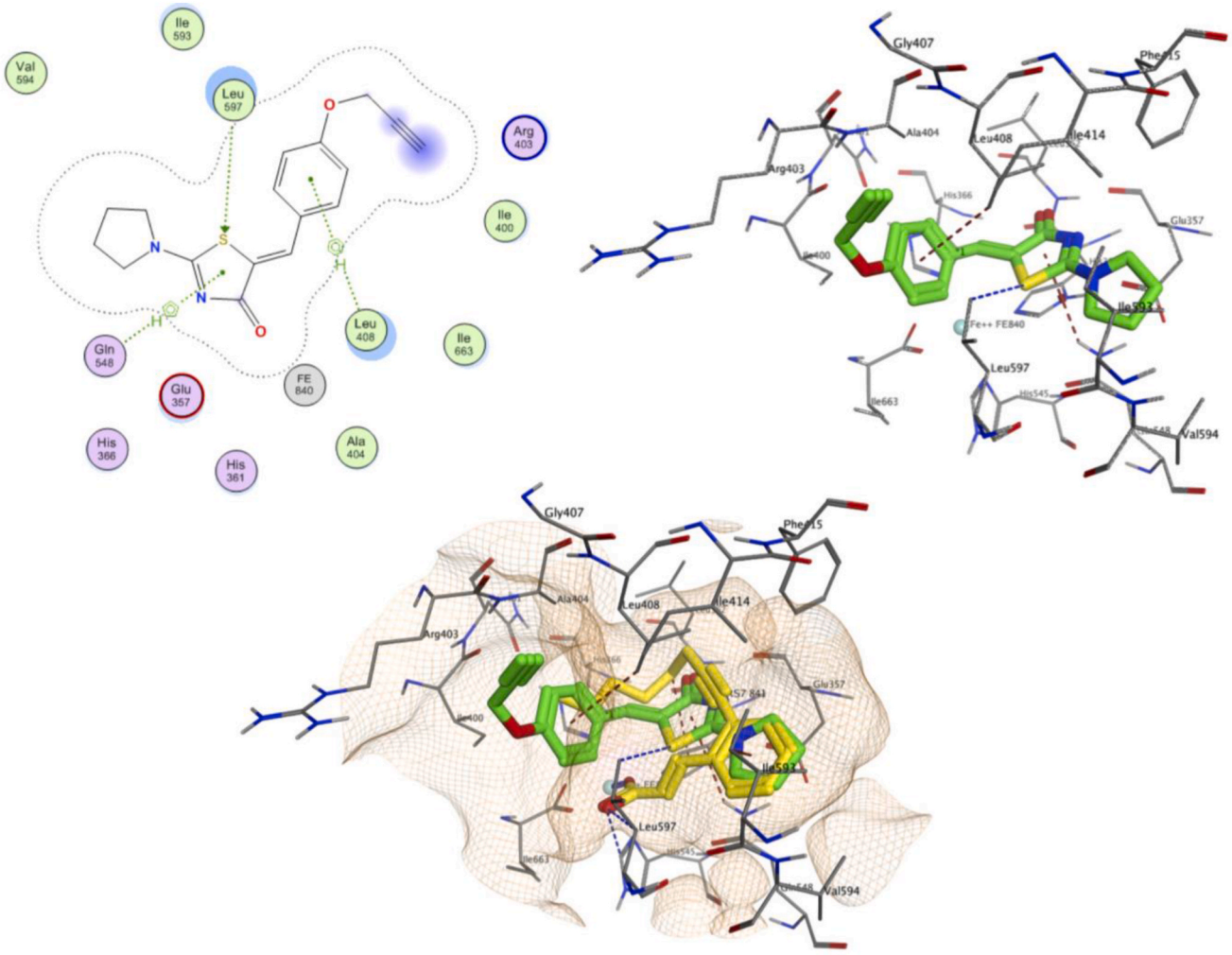

Fig. 10. Docking and binding pattern of compound **2a** inside the active site of 15-LOX (PDB ID: 1LOX) as follows: The best docked pose in 2D (left upper panel), 3D (right upper panel) and overlaid on the native ligand RS7 on a molecular surface (lower panel).

pioglitazone. Then, their PPARγ modulation in a Gal4-hybrid reporter gene assay was confirmed. In doing so, compound **2a** activated PPARγ with an EC_{50} value of 3.4 μM suggesting partial agonistic activity, which also echoed with its binding mode within the LBD of PPARγ in docking simulation study. Compound **2a** was also docked into COX-2 and 15-LOX active sites and exhibited adequate binding modes and affinities, thereby giving credence to their biological *in vitro* activities. As well, the expression levels of 20-HETE, Il-1β and TNF-α were decreased in LPS-challenged RAW264.7 macrophages upon treatment with compound **2a**. Prior to the *in vivo* evaluation of the efficacy of compound **2a**, a pharmacokinetic study was undertaken, revealing that the measured parameters were within an acceptable range, thus, justifying the dose selection for the animal model experiment. The latter was carried out in rat models of metabolic impairment where results revealed a reduction in hepatic malondialdehyde levels, as a lipid peroxidation marker, as well as pro-inflammatory cytokines production in the diabetic group. Similarly, a systemic anti-inflammatory effect was clearly observed with an increase in total antioxidant capacity in both prediabetic and diabetic groups. Consequently, this series of compounds proved their appropriateness as lead-like entities for the management of metabolic diseases-associated liver inflammation.

It is worth highlighting that compound **2a** and **Lead structure 1** possessed comparable activities in terms of COX-2, 15-LOX inhibition (IC_{50} values operating within the same order of magnitude) as well as PPARγ partial agonism. Nonetheless, **Lead structure 1** was identified as an insulin-dependent glucose uptake enhancer whereas the newly designed structural modification in **2a** resulted in a possible mixed agonist/antagonist response as it exerted considerably higher glucose uptake activity in absence of insulin, and a lower uptake in its presence. Given the different animal models employed to assess the *in vivo* efficacy of both compounds, it is noteworthy to point out that the study reporting **lead structure 1** was mainly directed towards the evaluation of the general anti-inflammatory activity of this MTDL via a formalin-induced rat paw edema model, which was successfully validated. However, and in order to extend the *in vivo* applicability of the same target combination, a new subset of compounds was designed, featuring a carefully chosen structural modification (relying on **lead structure 2**), to explore its potential in a different animal model of metabolic disease. The most active compound of which (**2a**) proved to ameliorate liver inflammation as a critical component of early-stage metabolic diseases. In addition, its antioxidant capacity was proven reflecting the known potential of PPARγ to alleviate oxidative stress in NASH. Besides, compound **2a** was shown to have a favorable *in vivo* pharmacokinetic profile in rats.

4. Experimental

4.1. Chemistry

All chemicals were acquired commercially and used directly without further purification. Melting points were recorded on electrotherm

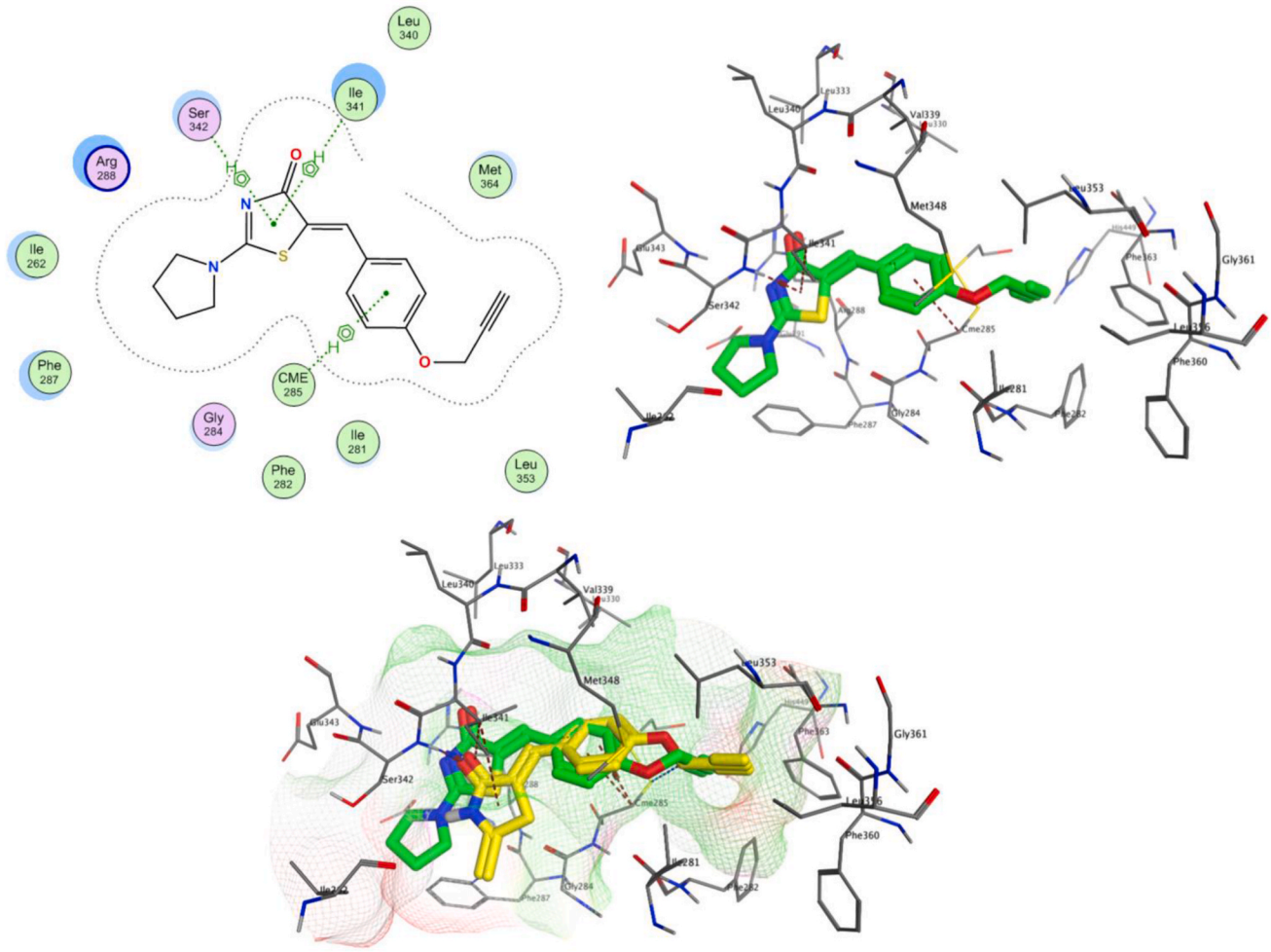

Fig. 11. Docking and binding pattern of compound **2a** inside the LBD of PPARγ (PDB ID: 5E5A) as follows: The best docked pose in 2D (left upper panel), 3D (right upper panel) and overlaid on the native ligand HV4 on a molecular surface (lower panel).

capillary tube Stuart melting point apparatus SMP10 and are all uncorrected. Follow up of the reactions' rates were performed by thin-layer chromatography (TLC) on silica gel-precoated aluminum sheets (Type 60 GF254; Merck; Germany) and the spots were visualized by exposure to iodine vapors or UV-lamp at λ 254 nm for few seconds. Infrared spectra (IR) were recorded using KBr discs on a PerkinElmer IR spectrophotometer, at the Microanalytical Unit, Faculty of Pharmacy, Mansoura University. Nuclear magnetic resonance (^{1}H NMR and ^{13}C NMR) spectra were recorded on a Joel JNM ECA 500II (500 MHz) spectrometer at the Faculty of Science; Mansoura University, and on a Bruker Avance III (400 MHz) spectrophotometer (Bruker AG, Switzerland) with BBFO Smart Probe and Bruker 400 AEON Nitrogen-Free Magnet, at the Faculty of Pharmacy; Beni Suef university, using deuterated dimethylsulfoxide (DMSO-d_6) as solvent. The data were recorded as chemical shifts expressed in δ (ppm) relative to tetramethylsilane (TMS) as internal standard. Signal splitting is expressed by the following abbreviations: s = singlet, d = doublet, t = triplet, q = quartet and m = multiplet. Purity of the new compounds was assessed by elemental analyses (C, H, N and S) and carried out on FLASH 2000 CHNS/O analyzer, Thermo Scientific at the regional center for mycology and biotechnology (RCMB), Al-Azhar University. The results were within ±0.4 % of the calculated values for the proposed formulae. Preparation of the propargyl intermediates **1a,b** and **3a,b** [47–51], was achieved as previously reported.

4.1.1. General procedure for the preparation of (Z)-5-benzylidene thiazol-4(5H)-one (2a-f and 4a-f)

The appropriate aldehyde **1a, 1b, 3a** or **3b** (1.5 mmol), rhodanine (0.13 g, 1 mmol) and cyclic secondary amine (1.5 mmol) were mixed in absolute ethanol (10 mL), in the presence of catalytic amount of glacial acetic acid and refluxed for 8–12 h. The product, which precipitated overnight after cooling to room temperature, was filtered, washed with cold ethanol and dried. It was then crystallized from ethanol or dioxane to yield the appropriate solid products.

*4.1.1.1. (Z)-5-(4-(Prop-2-yn-1-yloxy)benzylidene)-2-(pyrrolidin-1-yl) thiazol-4(5H)-one (**2a**).* Shiny yellow needles, yield 88 %. m.p. 220–222 °C. IR (KBr, cm^{-1}): 3217 (C≡CH), 2917 (aliphatic C–H), 2126 (C≡C), 1673 (C═O), 1595 (C═N), 1247 (C–*O*–C). ^{1}H NMR (400 MHz, DMSO-d_6): δ 1.98–2.03 (m, 4H, pyrrolidine-$C_{3,4}$-H), 3.60–3.69 (m, 5H, pyrrolidine-$C_{2,5}$-H and C≡CH), 4.88 (d, J = 2.4 Hz, 2H, OCH_2), 7.12 (d, J = 8.8 Hz, 2H, Aryl-$C_{3,5}$-H), 7.58 (d, J = 8.8 Hz, 2H, Aryl-$C_{2,6}$-H), 7.59 (s, 1H, arylidene = CH). ^{13}C NMR (100 MHz, DMSO-d_6): δ 25.0, 25.2, 49.2, 51.0, 56.1, 79.1, 79.3, 116.0, 127.1, 127.5, 129.9, 131.6, 158.7, 171.5, 179.4. Anal. Calcd (%) for $C_{17}H_{16}N_2O_2S$ (312.39): C, 65.36; H, 5.16; N, 8.97; S, 10.26. Found: C, 65.52; H, 5.39; N, 9.12; S, 10.34.

*4.1.1.2. (Z)-2-(Piperidin-1-yl)-5-(4-(prop-2-yn-1-yloxy)benzylidene)thiazol-4(5H)-one (**2b**).* Yellow powder, yield 70 %. m.p. 201–203 °C. IR (KBr, cm^{-1}): 3284 (C≡CH), 2941 (aliphatic C–H), 2128 (C≡C), 1676 (C═O), 1611 (C═N), 1255 (C–*O*–C). ^{1}H NMR (400 MHz, DMSO-d_6): δ

1.62–1.68 (m, 6H, piperidine-$C_{3,4,5}$-H), 3.61–3.91 (2 m, 5H, piperidine-$C_{2,6}$-H and C ≡ CH), 4.88 (d, J = 2 Hz, 2H, OCH_2), 7.11 (d, J = 8.8 Hz, 2H, Aryl-$C_{3,5}$-H), 7.59 (m, 2H, Aryl-$C_{2,6}$-H), 7.61 (s, 1H, arylidene = CH). ^{13}C NMR (100 MHz, DMSO-d_6): δ 23.9, 25.6, 26.2, 49.5, 50.3, 56.1, 79.1, 79.3, 116.0, 126.8, 127.5, 129.8, 131.7, 158.7, 173.7, 180.1. Anal. Calcd (%) for $C_{18}H_{18}N_2O_2S$ (326.41): C, 66.23; H, 5.56; N, 8.58; S, 9.82. Found: C, 66.16; H, 5.70; N, 8.76; S, 10.01.

4.1.1.3. (Z)-2-Morpholino-5-(4-(prop-2-yn-1-yloxy)benzylidene)thiazol-4(5H)-one ***(2c)***. Off-white powder, yield 71 %. m.p. 232–234 °C. IR (KBr, cm^{-1}): 3242 (C ≡ CH), 2912 (aliphatic C–H), 2127 (C ≡ C), 1677 (C═O), 1609 (C═N), 1247 (C–*O*–C). ^{1}H NMR (400 MHz, DMSO-d_6): δ 3.62 (m, 1H, C ≡ CH), 3.67–3.94 (3 m, 8H, morpholine-$C_{2,3,5,6}$-H), 4.89 (d, J = 2.4 Hz, 2H, OCH_2), 7.12 (d, J = 8.8 Hz, 2H, Aryl-$C_{3,5}$-H), 7.60 (m, 2H, Aryl-$C_{2,6}$-H), 7.63 (s, 1H, arylidene = CH). ^{13}C NMR (100 MHz, DMSO-d_6): δ 48.8, 49.0, 56.1, 66.0, 66.1, 79.1, 79.3, 116.1, 126.3, 127.4, 130.3, 131.8, 158.8, 174.8, 179.8. Anal. Calcd (%) for $C_{17}H_{16}N_2O_3S$ (328.39): C, 62.18; H, 4.91; N, 8.53; S, 9.76. Found: C, 62.40; H, 4.83; N, 8.75; S, 9.82.

4.1.1.4. (Z)-5-(3-Methoxy-4-(prop-2-yn-1-yloxy)benzylidene)-2-(pyrrolidin-1-yl)thiazol-4(5H)-one ***(2d)***. Green needles, yield 80 %. m.p.214–216 °C. IR (KBr, cm^{-1}): 3174 (C ≡ CH), 2954 (aliphatic C–H), 2118 (C ≡ C), 1680 (C═O), 1572 (C═N), 1242 (C–*O*–C). ^{1}H NMR (400 MHz, DMSO-d_6): δ 1.97–2.02 (m, 4H, pyrrolidine-$C_{3,4}$-H), 3.61–3.69 (m, 5H, pyrrolidine-$C_{2,5}$-H and C ≡ CH), 3.83 (s, 3H, OCH_3), 4.87 (d, J = 2 Hz, 2H, OCH_2), 7.17 (m, 2H, Aryl-$C_{5,6}$-H), 7.23 (s, 1H, Aryl-C_2-H), 7.58 (s, 1H, arylidene = CH). ^{13}C NMR (100 MHz, DMSO-d_6): δ 25.0, 25.2, 49.2, 51.0, 56.1, 56.5, 79.1, 79.4, 113.9, 114.5, 122.5, 127.4, 128.0, 130.3, 148.2, 149.7, 171.5, 179.4. Anal. Calcd (%) for $C_{18}H_{18}N_2O_3S$ (342.41): C, 63.14; H, 5.30; N, 8.18; S, 9.36. Found: C, 63.43; H, 5.17; N, 8.42; S, 9.50.

4.1.1.5. (Z)-5-(3-Methoxy-4-(prop-2-yn-1-yloxy)benzylidene)-2-(piperidin-1-yl)thiazol-4(5H)-one ***(2e)***. Brown crystals, yield 68 %. m.p. 178–180 °C. IR (KBr, cm^{-1}): 3224 (C ≡ CH), 2933 (aliphatic C–H), 2124 (C ≡ C), 1675 (C═O), 1614 (C═N), 1260 (C–*O*–C). ^{1}H NMR (400 MHz, DMSO-d_6): δ 1.62–1.67 (m, 6H, piperidine-$C_{3,4,5}$-H), 3.61–3.91 (m, 5H, piperidine-$C_{2,6}$-H and C ≡ CH), 3.84 (s, 3H, OCH_3), 4.87 (d, J = 2 Hz, 2H, OCH_2), 7.14–7.21 (m, 2H, Aryl-$C_{5,6}$-H), 7.23 (s, 1H, Aryl-C_2-H), 7.59 (s, 1H, arylidene = CH). ^{13}C NMR (100 MHz, DMSO-d_6): δ 23.9, 25.6, 26.2, 49.5, 50.2, 56.1, 56.5, 79.1, 79.4, 113.8, 114.4, 122.8, 127.1, 128.0, 130.2, 148.3, 149.8, 173.8, 180.0. Anal. Calcd (%) for $C_{19}H_{20}N_2O_3S$ (356.44): C, 64.02; H, 5.66; N, 7.86; S, 8.99. Found: C, 64.29; H, 5.84; N, 8.03; S, 9.12.

4.1.1.6. (Z)-5-(3-Methoxy-4-(prop-2-yn-1-yloxy)benzylidene)-2-morpholinothiazol-4(5H)-one ***(2f)***. Yellow crystals, yield 83 %. m.p. 186–188 °C. IR (KBr, cm^{-1}): 3250 (C ≡ CH), 2922 (aliphatic C–H), 2126 (C ≡ C), 1665 (C═O), 1594 (C═N), 1271 (C–*O*–C). ^{1}H NMR (400 MHz, DMSO-d_6): δ 3.61 (t, J = 2 Hz, 1H, C ≡ CH), 3.68–3.94 (m, 8H, morpholine-$C_{2,3,5,6}$-H), 3.84 (s, 3H, OCH_3), 4.88 (d, J = 2 Hz, 2H, OCH_2), 7.15–7.26 (m, *3*H, Aryl-$C_{2,5,6}$-H), 7.63 (s, 1H, arylidene = CH). ^{13}C NMR (100 MHz, DMSO-d_6): δ 48.8, 49.0, 56.1, 56.5, 66.0, 66.1, 79.1, 79.4, 113.8, 114.4, 122.9, 126.6, 127.9, 130.7, 148.4, 149.8, 174.8, 179.8. Anal. Calcd (%) for $C_{18}H_{18}N_2O_4S$ (358.41): C, 60.32; H, 5.06; N, 7.82; S, 8.95. Found: C, 60.54; H, 5.22; N, 8.06; S, 9.01.

4.1.1.7. (Z)-5-(3-(Prop-2-yn-1-yloxy)benzylidene)-2-(pyrrolidin-1-yl)thiazol-4(5H)-one ***(4a)***. Light brown powder, yield 68 %. m.p. 168–170 °C. IR (KBr, cm^{-1}): 3156 (C ≡ CH), 2969 (aliphatic C–H), 2108 (C ≡ C), 1683 (C═O), 1609 (C═N), 1263 (C–*O*–C). ^{1}H NMR (400 MHz, DMSO-d_6): δ 1.97–2.05 (m, 4H, pyrrolidine-$C_{3,4}$-H), 3.61–3.72 (m, 5H, pyrrolidine-$C_{2,5}$-H and C ≡ CH), 4.87 (d, J = 2 Hz, 2H, OCH_2), 7.07 (m, 1H, Aryl-C_4-H), 7.23 (m, 2H, Aryl-$C_{2,6}$-H), 7.44 (t, J = 8.2 Hz, 1H, Aryl-C_5-H), 7.59 (s, 1H, arylidene = CH). ^{13}C NMR (100 MHz, DMSO-d_6): δ 25.0, 25.2, 49.3, 51.1, 56.1, 79.1, 79.5, 116.2, 116.7, 122.7, 129.9, 130.1, 130.8, 135.8, 158.1, 171.6, 179.1. Anal. Calcd (%) for $C_{17}H_{16}N_2O_2S$ (312.39): C, 65.36; H, 5.16; N, 8.97; S, 10.26. Found: C, 65.51; H, 5.08; N, 8.76; S, 9.91.

4.1.1.8. (Z)-2-(Piperidin-1-yl)-5-(3-(prop-2-yn-1-yloxy)benzylidene)thiazol-4(5H)-one ***(4b)***. Beige powder, yield 65 %. m.p. 139–141 °C. IR (KBr, cm^{-1}): 3203 (C ≡ CH), 2939 (aliphatic C–H), 2111 (C ≡ C), 1679 (C═O), 1607 (C═N), 1292 (C–*O*–C). ^{1}H NMR (400 MHz, DMSO-d_6): δ 1.62–1.68 (m, 6H, piperidine-$C_{3,4,5}$-H), 3.62–3.91 (2 m, 5H, piperidine-$C_{2,6}$-H and C ≡ CH), 4.87 (d, J = 2 Hz, 2H, OCH_2), 7.07 (m, 1H, Aryl-C_4-H), 7.24 (m, 2H, Aryl-$C_{2,6}$-H), 7.43 (t, J = 8 Hz, 1H, Aryl-C_5-H), 7.60 (s, 1H, arylidene = CH). ^{13}C NMR (100 MHz, DMSO-d_6): δ 23.9, 25.6, 26.2, 49.6, 50.4, 56.0, 79.0, 79.5, 116.2, 116.7, 122.8, 129.7, 129.8, 130.7, 135.8, 158.0, 173.7, 179.7. Anal. Calcd (%) for $C_{18}H_{18}N_2O_2S$ (326.41): C, 66.23; H, 5.56; N, 8.58; S, 9.82. Found: C, 65.87; H, 5.70; N, 8.80; S, 9.94.

4.1.1.9. (Z)-2-Morpholino-5-(3-(prop-2-yn-1-yloxy)benzylidene)thiazol-4(5H)-one ***(4c)***. Beige powder, yield 70 %. m.p. 169–171 °C. IR (KBr, cm^{-1}): 3263 (C ≡ CH), 2926 (aliphatic C–H), 2117 (C ≡ C), 1685 (C═O), 1610 (C═N), 1283 (C–*O*–C). ^{1}H NMR (400 MHz, DMSO-d_6): δ 3.61 (m, 1H, C ≡ CH), 3.67–3.94 (3 m, 8H, morpholine-$C_{2,3,5,6}$-H), 4.86 (d, J = 2.4 Hz, 2H, OCH_2), 7.07 (m, 1H, Aryl-C_4-H), 7.23 (m, 2H, Aryl-$C_{2,6}$-H), 7.44 (t, J = 8.4 Hz, 1H, Aryl-C_5-H), 7.62 (s, 1H, arylidene = CH). ^{13}C NMR (100 MHz, DMSO-d_6): δ 48.9, 49.1, 56.1, 66.0, 66.1, 79.0, 79.5, 116.2, 116.8, 122.9, 129.3, 130.4, 130.8, 135.7, 158.1, 174.9, 179.6. Anal. Calcd (%) for $C_{17}H_{16}N_2O_3S$ (328.39): C, 62.18; H, 4.91; N, 8.53; S, 9.76. Found: C, 62.49; H, 5.14; N, 8.66; S, 9.81.

4.1.1.10. (Z)-5-(4-Methoxy-3-(prop-2-yn-1-yloxy)benzylidene)-2-(pyrrolidin-1-yl)thiazol-4(5H)-one ***(4d)***. Yellow crystals, yield 82 %. m.p. 225–227 °C. IR (KBr, cm^{-1}): 3255 (C ≡ CH), 2915 (aliphatic C–H), 2128 (C ≡ C), 1676 (C═O), 1596 (C═N), 1264 (C–*O*–C). ^{1}H NMR (400 MHz, DMSO-d_6): δ 1.97–2.06 (m, 4H, pyrrolidine-$C_{3,4}$-H), 3.61–3.72 (m, 5H, pyrrolidine-$C_{2,5}$-H and C ≡ CH), 3.84 (s, 3H, OCH_3), 4.86 (d, J = 2.4 Hz, 2H, OCH_2), 7.14 (d, J = 8.4 Hz, 1H, Aryl-C_5-H), 7.25 (dd, J = 8.4 Hz, 1H, Aryl-C_6-H), 7.32 (s, 1H, Aryl-C_2-H), 7.56 (s, 1H, arylidene = CH). ^{13}C NMR (100 MHz, DMSO-d_6): δ 25.0, 25.2, 49.2, 51.0, 56.2, 56.7, 79.2, 79.5, 113.0, 115.7, 124.4, 126.9, 127.1, 130.3, 147.1, 151.1, 171.6, 179.4. Anal. Calcd (%) for $C_{18}H_{18}N_2O_3S$ (342.41): C, 63.14; H, 5.30; N, 8.18; S, 9.36. Found: C, 62.96; H, 5.43; N, 8.42; S, 9.52.

4.1.1.11. (Z)-5-(4-Methoxy-3-(prop-2-yn-1-yloxy)benzylidene)-2-(piperidin-1-yl)thiazol-4(5H)-one ***(4e)***. Shiny yellow crystals, yield 66 %. m.p. 176–178 °C. IR (KBr, cm^{-1}): 3263 (C ≡ CH), 2941 (aliphatic C–H), 2125 (C ≡ C), 1677 (C═O), 1559 (C═N), 1262 (C–*O*–C). ^{1}H NMR (400 MHz, DMSO-d_6): δ 1.61–1.68 (m, 6H, piperidine-$C_{3,4,5}$-H), 3.61–3.91 (m, 5H, piperidine-$C_{2,6}$-H and C ≡ CH), 3.84 (s, 3H, OCH_3), 4.86 (m, 2H, OCH_2), 7.11–7.31 (m, 3H, Aryl-$C_{2,5,6}$-H), 7.56 (s, 1H, arylidene = CH). ^{13}C NMR (100 MHz, DMSO-d_6): δ 23.9, 25.6, 26.2, 49.5, 50.2, 56.2, 56.7, 79.2, 79.5, 112.9, 115.5, 124.5, 126.8, 130.1, 147.1, 151.1, 173.8, 180.0. Anal. Calcd (%) for $C_{19}H_{20}N_2O_3S$ (356.44): C, 64.02; H, 5.66; N, 7.86; S, 8.99. Found: C, 63.87; H, 5.80; N, 8.09; S, 8.85.

4.1.1.12. (Z)-5-(4-Methoxy-3-(prop-2-yn-1-yloxy)benzylidene)-2-morpholinothiazol-4(5H)-one ***(4f)***. Off-white crystals, yield 81 %. m.p. 210–212 °C. IR (KBr, cm^{-1}): 3262 (C ≡ CH), 2928 (aliphatic C–H), 2117 (C ≡ C), 1682 (C═O), 1601 (C═N), 1274 (C–*O*–C). ^{1}H NMR (400 MHz, DMSO-d_6): δ 3.62–3.93 (3 m, 9H, morpholine-$C_{2,3,5,6}$-H and C ≡ CH), 3.84 (s, 3H, OCH_3), 4.86 (d, J = 2.4 Hz, 2H, OCH_2), 7.12 (d, J = 8.4 Hz, 1H, Aryl-C_5-H), 7.25–7.31 (m, 2H, Aryl-$C_{2,6}$-H), 7.59 (s, 1H, arylidene = CH). ^{13}C NMR (100 MHz, DMSO-d_6): δ 48.7, 49.0, 56.2, 56.7, 66.0, 66.1, 79.2, 79.5, 112.9, 115.5, 124.7, 126.3, 126.7, 130.7, 147.1, 151.2,

174.9, 179.8. Anal. Calcd (%) for $C_{18}H_{18}N_2O_4S$ (358.41): C, 60.32; H, 5.06; N, 7.82; S, 8.95. Found: C, 60.63; H, 5.13; N, 8.17; S, 9.07.

4.2. Biological evaluation

4.2.1. In vitro COX-1/2 and 15-LOX inhibition assays

Both the COX-1/2 and the soya bean 15-LOX inhibitory activities were measured with assay kits from Cayman Chemicals, Ann Arbor, MI, USA. The colorimetric COX (ovine) inhibitor screening assay kit (Catalog No. 560131) and the lipoxygenase inhibitor screening assay kit (Catalog No. 760700) were used for this purpose. Consistent with our prior work, we followed the manufacturer's instructions while preparing the reagents and conducting the tests to determine the IC_{50} values of the compounds under investigation [22,52].

4.2.2. In vitro glucose uptake using rat hemi-diaphragm model

The methods for animal use and care were in adherence to the US National Institute of Health's Guide for the Care and Use of Laboratory Animals (NIH publication No. 83–23, amended in 1996), together with Alexandria University's laboratory animal ethical guidelines. All experiments included appropriate precautions to decrease animal pain or discomfort. Measurement of the *in vitro* glucose uptake activity was undertaken according to the rat hemi-diaphragm method described previously [53,54]. Wistar rats were maintained on a standard pellet diet, water *ad libitum*, and fastened for an overnight before being sacrificed and euthanized under isoflurane anesthesia. The diaphragms of Wistar rats were quickly removed (avoiding trauma and commotion) and split into two equal halves. Following that, the hemi-diaphragms were rinsed in cold Tyrode solution (without glucose) to clear any blood clots and then transferred to the respective wells. The closed plates were incubated at 21 °C and shaken at a rate of 60 cycles per minute for 45 min. Following incubation, the glucose content of the working solutions was determined using the VITRO SCIENT glucose kit and applying the GOD/POD enzymatic method. Glucose uptake was determined as the difference between the initial and final glucose contents in the incubated media. The working solutions were divided into 28 groups. The first and second groups acted as negative controls containing 2 mL of Tyrode solution and 2000 mg/L glucose with and without 5 μL (0.2 IU) of regular insulin (Novo Nordisk, 40 IU/mL). The third and fourth groups represented positive controls and contained the same as group one and two in addition to 2 mg of pioglitazone (as the standard drug). Groups 5–28 contained 2 mL of Tyrode solution with 2000 mg/L glucose and 2 mg of the test compounds **2a-2f** and **4a-4f** with and without 5 μL of regular insulin (Novo Nordisk, 40 IU/mL).

4.2.3. KEGG pathways enrichment analysis

For the target fishing study, compound **2a** was submitted to pharmmapper server (https://www.lilab-ecust.cn/pharmmapper/) [55], and Passonline tool (Prediction of Activity Spectra for Substances) (https://www.way2drug.com/passonline/) [56] which estimates potential targets/activities based on probabilities of activity Pa and inactivity Pi. Then, all targets from pharmmapper were referred to Venn tool (https://bioinformatics.psb.ugent.be/webtools/Venn/) to extract the targets that are shared with targets relevant to NAFLD or NASH from disgenet database (https://www.disgenet.com/). The resultant genes were then subjected to KEGG pathway enrichment analysis using ShinyGO 0.80 tool (http://bioinformatics.sdstate.edu/go/) [57].

4.2.4. Gal4-PPARγ reporter gene assay

PPARγ activation was determined as described previously [58]. In brief, HEK293T cells (German Collection of Microorganisms and Cell Culture GmbH, DSMZ) were cultured in Dulbecco's modified Eagle's medium (DMEM), high glucose supplemented with 10 % fetal calf serum (FCS), sodium pyruvate (1 mM), penicillin (100 U/mL), and streptomycin (100 mg/mL) at 37 °C and 5 % CO_2 and seeded in 96-well plates ($3*10^4$ cells/well) 24 h prior to transfection. Before transfection, medium was changed to Opti-MEM without supplements and cells were transiently transfected using Lipofectamine LTX reagent (Invitrogen, Carlsbad, CA, USA) with pFR-Luc (Stratagene, La Jolla, CA, USA), pRL-SV40 (Promega, Madison, WI, USA) and pFA-CMV-hPPARγ-LBD. Five hours after transfection, cells were incubated with the test compounds at varying concentrations in Opti-MEM supplemented with penicillin (100 U/mL), streptomycin (100 mg/mL) and 0.1 % DMSO or with the medium as untreated control. Each concentration was tested in duplicates and each experiment was repeated independently at least three times. After 16 h incubation, cells were assayed for luciferase activity using the Dual-Glo Luciferase Assay System (Promega) and luminescence was measured with a Tecan Spark luminometer (Tecan Deutschland GmbH, Germany). Firefly luciferase data were normalized to Renilla luciferase data to account for transfection efficiency and cell growth. Fold activation was obtained by normalizing the effect of a test sample to untreated cells (medium with 0.1 % DMSO) and relative activation was obtained by normalizing the fold activation data of a test sample to the effect of 1 μM pioglitazone as the positive control. EC_{50} values were calculated in GraphPad Prism (version 7.00, GraphPad Software, La Jolla, CA) using mean relative activation values ± SD and the equation " [Agonist] versus response (three parameters)".

4.2.5. In vitro examination of the effect of compound 2a on the expression of inflammatory mediators in lipopolysaccharide-stimulated macrophages

RAW264.7 macrophage cells, obtained from the American Type Culture Collection (Manassas, VA, USA), were cultivated in Dulbecco's modified Eagle's medium (DMEM) with 10 % fetal bovine serum (FBS) added (General Electric Healthcare Life), and containing 1 % Penicillin streptomycin (P/S 100 U/ml and 100 mg/ml, respectively, Solarbio life sciences, Beijing, P. R. China) at 37 °C and 5 % CO_2. MTT assay was used to determine the effect of each of **2a** and celecoxib on cell viability. RAW 264.7 macrophages were plated at a density of $5*10^5$ cells/mL in a 96-well plate, with different concentrations of the compounds dissolved in DMSO and incubated for 48 h. Briefly for the cell proliferation assay, the MTT labeling mixture was prepared by mixing 50 vol 1 mg/mL sodium 30-[1-(phenylaminocarbonyl)-3,4-tetrazolium]-bis(4-methoxy-6-nitro) benzene sulfonic acid hydrate (in media) with 1 vol 0.383 mg/mL N-methyldibenzopyrazine methyl sulfate in PBS. This mixture was added to the cultures and incubated for 1 h at 37 °C. Absorbance was measured at 490 nm with a reference wavelength at 650 nm. Recorded IC_{50} values were 293.15 ± 14.9 and 151.16 ± 7.69 μg/mL for compound **2a** and celecoxib, respectively. The highest drug concentration sustaining over 80 % cell activity was utilized for the following step as previously described [59]. For the determination of the effect on inflammatory mediators, RAW 264.7 cells were plated at a density of $5*10^5$ cells/mL in a 6-well plate, pretreated with **2a** and celecoxib (50 μg/ml) for 1 h, and stimulated with 1 μg/mL LPS for 48 h. Upon completion of the challenge period, the conditioned medium was harvested from the cell cultures in the 6-well plates, extracted, and the concentrations of 20-HETE, Il-1β and TNF-α were measured using the ELISA kits (20H39–K01-Eagle Biosciences), (ab214025), (ab208348) according to the manufacturer instructions, respectively [60].

4.2.6. In vivo experiments

4.2.6.1. Chemicals and drugs. Streptozotocin (STZ) was purchased from Sigma (St. Louis, MO, USA). The Pioglitazone used in this study was commercially available pharmaceutical grade Pioglitazone (October Pharma).

4.2.6.2. Animal studies. Forty male Sprague-Dawley rats (200–240 gm) were obtained from the animal house at the Institute of Graduate Studies and Research, Alexandria University, Egypt. The rats were housed in a temperature and humidity-controlled room in well-ventilated polypropylene cages, under a 12-h light-dark cycle with food and water *ad*

libitum. The animal experiment was done according to the ARRIVE guidelines and according to a protocol approved by the Animal Care and Use Committee of the Faculty of Pharmacy, Alexandria University (Approval number 06-2022-9-5-3-127).

4.2.6.3. Pharmacokinetic study. Five rats were used for preliminary pharmacokinetics of **2a** as described previously [34]. Briefly, rats were fasted overnight prior to the day of the experiment. On the day of the experiment, each rat received a single oral dose of 10 mg/kg of compound **2a** by oral gavage. Blood samples were collected at 0, 0.5, 1, 2, 4, 8, 12, and 24 h post administration. Plasma was separated by centrifugation and the concentration of the drug was determined as described below. The plasma concentration vs. time curve was plotted and non-linear regression (GraphPad Prism) was used to determine the AUC, C_{max}, and T_{max}. K_e and $t_{1/2}$ were determined from the best fit values of a one-phase decay function of the plasma concentration data at time points beyond T_{max}. K_a was determined using the methods of residuals [35]. The measured and computed parameters were used to estimate the average plasma concentration upon repeated oral administration (C_{Av}) as follows. First, the term (F/V_d) was determined for each of the selected test compounds from the below equation:

$$C = \frac{F \bullet D \bullet k_a}{Vd(k_a - k_c)} \bullet \left(e^{-k_e \bullet t} - e^{-k_a \bullet t}\right)$$

Where C is plasma concentration at time t, F is the oral dose fraction absorbed, Vd is the volume of distribution, and D is the oral dose. Afterwards, C_{Av} was calculated using the below equation:

$$C_{Av} = \frac{F \bullet D}{k_e \bullet V_d \bullet \tau}$$

Where τ is the dosing interval being 24 h in our protocol.

*4.2.6.4. Chromatographic determination of plasma **2a** concentration using LC-MS/MS.* All reagents used were HPLC high pure grade from the indicated source: Acetonitrile (Sigma Aldrich™ hypergrade for LC-MS), Formic acid (Fischer™ HPLC grade), and Ultrapure water (Stakpure Omnia xs™ water system). The chromatographic system consists of: Thermo Fischer Vanquish Horizon UHPLC system combined with TSQ Fortis™ Plus Triple Quadrupole Mass Spectrometer and TraceFinder™ 5.1 software. The column used for separation was Hypersil GOLD™ (5 μm, 150 × 4 mm). Plasma samples were stored at −20 °C till the time of analysis within 48 h. At the time of analysis, samples were defrosted at room temperature then 100 μL were treated with 200 μL Acetonitrile for protein precipitation, mixed by vortex, then centrifuged at 20,000 rpm at 9 °C for 20 min 10 μL of the clear supernatant solutions were injected into the LC system. Chromatographic separation was achieved using an isocratic flow of a mixture of 40 % acetonitrile in 0.1 % formic acid aqueous solution with a 0.8 mL/min flow rate. The column and autosampler temperatures were maintained at 30 °C and 9 °C respectively.

Calibration standards were prepared by spiking different concentrations of the tested compound to a blank plasma matrix equivalent to 15, 30, 45, 75, 150, 300, and 600 ng drug compound per 1 mL plasma, then treated as plasma samples. The calibration set was used to partially validate the analytical method for linearity and accuracy, and a blank plasma sample was used to validate the specificity of the method. The detection of the sought compound was achieved using selective reaction monitoring (SRM) of the ion molecular peak and at least two daughter peaks for quantitation (target) and confirmation at positive electrospray ionization mode (ESI).

4.2.6.5. Experimental design. Rats were randomly allocated into seven different groups of five rats each. (I) The control: rats were fed a normal chow diet, (II) the prediabetic (Pre D) group; rats were fed a hypercaloric diet, (III) the Pre D Pio group: rats were fed a hypercaloric diet and treated with oral pioglitazone (2 mg/kg/day), (IV) Pre D **2a** group: rats were fed a hypercaloric diet and treated with compound **2a** (10 mg/kg/day) orally, (V) Type 2 diabetic (D) rats: rats were fed a hypercaloric diet and received a 40 mg/kg streptozotocin intraperitoneal injection dissolved in citrate buffer at the beginning of weeks 9 and 10 [25], (VI) D Pio: diabetic rats treated with oral pioglitazone (2 mg/kg/day), (VII) D 2a: diabetic rats treated with compound **2a** (10 mg/kg/day) orally. Both pioglitazone and **2a** were administered as 0.25 % CMC suspension [61].

The hypercaloric diet was prepared in the house as described in our previous work [24,25,30]. Rats were fed a hypercaloric diet for 12 weeks and all treatments were given daily during the final two weeks, week 11 and 12. Body weight was measured weekly. All rats were euthanized at the end of the treatment period with an inhaled overdose of isoflurane, followed by exanguination. Blood and liver were collected then stored at −80 for further investigations.

The selected dose of pioglitazone was shown in our previous work to produce a consistent anti-inflammatory effect in different tissues and organs in metabolically challenged rats without a concurrent hypoglycemic effect [24,25,31]. As for **2a**, the initial dose selection was based on using an oral dose less than 1/20 of the predicted LD_{50} [32] (https://tox.charite.de/protox3/#) [33]. The dose was further confirmed based on the results of the pharmacokinetic study.

4.2.6.6. Blood chemistry parameters. Fasting blood sugar level was measured by a Contour ™ Plus glucometer (Ascensia Diabetes Care Holding AG, Basel, Switzerland) by lateral tail vein puncture for the first time to all rats, then before the first and second STZ injections as well as after 72 h of the injections for the diabetic groups only and again for all rats at week 11, 12 and on euthanization day. Tumor necrosis factor alpha (TNFα), interleukin-1β (IL1β), and Transforming growth factor-β (TGFβ) were measured in serum by ELISA kits (catalog numbers CSB-E11987r CUSABIO USA, E-EL-R0012 Elabscience USA, CSB-E04727r CUSABIO USA, respectively) according to the manufacturer's protocol. Total antioxidant capacity was measured by colorimetry using an ab65329 total antioxidant capacity assay kit.

4.2.6.7. Determination of malondialdehyde (MDA) using TBARS assay. Determination of MDA level was done on liver homogenates using Lipid Peroxidation (MDA) Assay Kit (Sigma-Aldrich, cat. No. MAKO85).

4.2.6.8. Determination of TNFα, IL-1β, and TGFβ expression in liver tissues using quantitative real-time polymerase chain reaction. Total RNA was extracted from liver tissues using TRIzol™ Plus RNA Purification Kit (catalog number: 12,183,555, Thermo Fisher Scientific, USA). cDNA was reverse transcribed from RNA using Applied Biosystems™ High Capacity cDNA Reverse Transcription Kit (catalog number: 4,368,814, Thermo Fisher Scientific, USA). Quantitative real time PCR was performed to measure the expression of TNFα, IL-1β, and TGFβ using Maxima SYBR Green qPCR Master Mix (2X) (catalog number: #K0252, Thermo Scientific, USA). The reaction was run at 95° for 10 min, followed by 40 cycles at the same temperature for 15 s, then another 40 cycles at 60° for 30 s and finally at 72° for 30 s for 40 cycles. The primer sequences are listed in Table 4. The relative expression of each gene was calculated according to the threshold cycle (Ct) based on $2^{-\Delta\Delta ct}$ formula (4)

Table 4
Primer sequences used for quantitative real time PCR.

Gene	Forward primer	Reverse primer
TNFα	ACTACCAGCTATCCCCATCT	CTGGTCACCAAATCAGCATT
IL1β	GTTTGAGTCTGCACAGTTCC	AAGTCAACTATGTCCCGACC
TGFβ	GCCAGATCCTGTCCAAACTA	CTGTTGTACAAAGCGAGCAC
β-actin (Actb) (House keeping gene)	ATGTGGCTGAGGACTTTGATT	ATCTATGCCGTGGATACTTGG

4.2.7. Statistical analysis

GraphPad Prism v7.0 (GraphPad Prism Inc., La Jolla, CA, USA) was used for these assessments. Results are displayed as mean ± standard error of the mean and analyzed with the one-way ANOVA followed by the Tukey post-hoc test. Probability level (P) ≤ 0.05 was considered significant.

4.3. Molecular docking

Computer aided docking investigations were achieved using Molecular Operating Environment (MOE 2019.0102) software, developed by the Chemical Computing Group in Montreal, Canada, as previously described [59,62]. The X-ray crystallographic coordinates of the COX-2 enzyme (PDB code 1CX2), in complex with SC-558, and the 15-LOX enzyme (PDB code 1LOX), in complex with RS7, were collected from the Protein Data Bank. In addition, the crystal structure of the LBD of human PPARγ (PDB code 6E5A), in association with our lead compound 1, was used. Compound **2a**, in its *Z*-configuration, was equipped by the process of hydrogen addition, followed by the computation of partial charges and energy minimization using the Force Field MMFF94x. Furthermore, the proteins were prepared by excluding the repetitive chains, water molecules, and surfactants. The MOE QuickPrep feature was used to rectify structural abnormalities, perform 3D protonation, and calculate partial charges. The MOE Dock technique used the default process to identify the favorable binding positions of the investigated ligand. This was achieved by utilizing the triangle matcher as the placement method and London dG as the main scoring function. To enhance the accuracy of the results, an additional refinement phase was implemented using the rigid receptor approach together with the GBVI/WSA dG scoring function. This step was intended to prioritize poses that exhibited the strongest hydrophobic, ionic, and hydrogen-bond interactions with the protein. The output database included the scores of ligand-enzyme complexes measured in kilocalories per mole (kcal/mol). Subsequently, the obtained docking postures were visually inspected and the interactions with residues in the binding pocket were analyzed. Poses that fit well into the binding pocket and have high scores, while also exhibiting strong interactions between the ligand and enzyme, were chosen.

4.4. In silico estimation of physicochemical properties, drug likeness, pharmacokinetic profile (ADMET) and ligand efficiency metrics

The physicochemical and drug-likeness parameters of compound **2a** were predicted using SwissADME web service (http://www.swissadme.ch/) [63]. Pharmacokinetic (https://preadmet.webservice.bmdrc.org/adme/) and toxicological profiling (https://tox.charite.de/protox3/) [33], together with the estimation of ligand efficiency indices, were performed to assess the eligibility as lead/drug candidate.

CRediT authorship contribution statement

Mai S. El-Shoukrofy: Writing – original draft, Investigation. **Azza Ismail:** Supervision, Investigation. **Reem H. Elhamammy:** Writing – original draft, Investigation. **Sherien A. Abdelhady:** Investigation. **Rasha Nassra:** Investigation. **Monica S. Makkar:** Investigation. **Mahmoud A. Agami:** Investigation. **Ahmed Wahid:** Writing – review & editing. **Hisham A. Nematalla:** Investigation. **Minh Sai:** Methodology, Investigation. **Daniel Merk:** Methodology, Writing – review & editing, Visualization, Supervision. **Ahmed F. El-Yazbi:** Writing – original draft, Visualization, Methodology, Conceptualization. **Ahmed S.F. Belal:** Writing – review & editing, Writing – original draft, Visualization, Supervision, Funding acquisition, Conceptualization. **Ali H. Eid:** Writing – review & editing, Visualization, Supervision, Methodology, Funding acquisition, Conceptualization. **Perihan A. Elzahhar:** Writing – review & editing, Supervision, Methodology, Funding acquisition, Conceptualization.

Data availability

The data used for this manuscript are available in the article; further inquiries can be directed to the corresponding authors.

Funding

A significant portion of this work was supported by the Alexandria University Research Support Initiative “Alex-RSI” CALL -1, Egypt. Open access funding provided by Qatar National Library.

Declaration of competing interest

The authors declare that they have no known competing financial interests or personal relationships that could have appeared to influence the work reported in this paper.

Acknowledgments

We would like to thank Alexandria University in Egypt for the funding granted by the Research Support Initiative “Alex-RSI” CALL -1. Authors are also grateful to the Qatar National Library for providing Open access funding.

Appendix A. Supplementary data

Supplementary data to this article can be found online at https://doi.org/10.1016/j.ejmech.2025.117415.

Data availability

Data will be made available on request.

References

[1] K.K. Bhopale, M.P. Srinivasan, Therapeutics for metabolic dysfunction-associated fatty liver disease (MAFLD), Livers 3 (2023) 597–617, https://doi.org/10.3390/livers3040040.
[2] U. Dayal, S. Bansal, K. Aggarwal, S. Gautham, R. Singh, A. Authors Utkarsh Dayal, U. Soni, C. Chennupati, S. Gautham Kanagala, V. Gupta, R. Singh Munjal, R. Jain, S.G. Kanagala, R.S. Munjal, MAFLD: exploring the systemic effects beyond liver, J. Community Hosp. Intern. Med. Perspect. 15 (2025) 42, https://doi.org/10.55729/2000-9666.1426.
[3] P. Sangro, M. de la Torre Aláez, B. Sangro, D. D'Avola, Metabolic dysfunction–associated fatty liver disease (MAFLD): an update of the recent advances in pharmacological treatment, J. Physiol. Biochem. 79 (2023) 869–879, https://doi.org/10.1007/S13105-023-00954-4/TABLES/1.
[4] E.A. Rakha, L. Adamson, E. Bell, K. Neal, S.D. Ryder, P.V. Kaye, G.P. Aithal, Portal inflammation is associated with advanced histological changes in alcoholic and non-alcoholic fatty liver disease, J. Clin. Pathol. 63 (2010) 790–795, https://doi.org/10.1136/JCP.2010.079145.
[5] H. Yki-Järvinen, Non-alcoholic fatty liver disease as a cause and a consequence of metabolic syndrome, Lancet Diabetes Endocrinol. 2 (2014) 901–910, https://doi.org/10.1016/S2213-8587(14)70032-4.
[6] A. Tanveer, R. Ullah, S. Ullah, S. Hussain, C. Author, P. Emirates Military Hospital, P. anamtanveer, ETIOLOGY of hepatocellular carcinoma, special FOCUS ON fatty liver disease, insights, J.Health Rehabilitat. 3 (2025) 252–258, https://doi.org/10.71000/AR44M963.
[7] M. Peiseler, F. Tacke, Inflammatory mechanisms underlying nonalcoholic steatohepatitis and the transition to hepatocellular carcinoma, Cancers 13 (2021) 1–26, https://doi.org/10.3390/CANCERS13040730.
[8] V.L. Gadd, R. Skoien, E.E. Powell, K.J. Fagan, C. Winterford, L. Horsfall, K. Irvine, A.D. Clouston, The portal inflammatory infiltrate and ductular reaction in human nonalcoholic fatty liver disease, Hepatology 59 (2014) 1393–1405, https://doi.org/10.1002/HEP.26937.
[9] S.J. Keam, Resmetirom: first approval, Drugs 84 (2024) 729–735, https://doi.org/10.1007/S40265-024-02045-0.
[10] Z. Feng, J. Xiang, H. Liu, J. Li, X. Xu, G. Sun, R. Zheng, S. Zhang, J. Liu, S. Yang, Q. Xu, X. Wen, H. Yuan, H. Sun, L. Dai, Design, synthesis, and biological evaluation of triazolone derivatives as potent pparα/δDual agonists for the treatment of nonalcoholic steatohepatitis, J. Med. Chem. 65 (2022) 2571–2592, https://doi.org/10.1021/ACS.JMEDCHEM.1C02002/SUPPL_FILE/JM1C02002_SI_002.CSV.
[11] T. Khare, K. Liu, L.O. Chilambe, S. Khare, NAFLD and NAFLD related HCC: emerging treatments and clinical trials, Int. J. Mol. Sci. 26 (2025), https://doi.org/10.3390/IJMS26010306.

[12] J.M. Fraile, S. Palliyil, C. Barelle, A.J. Porter, M. Kovaleva, Non-alcoholic steatohepatitis (NASH) - a review of a crowded clinical landscape, driven by a complex disease, Drug Des. Dev. Ther. 15 (2021) 3997–4009, https://doi.org/10.2147/DDDT.S315724.
[13] F. Chen, Q. Liu, L. Ma, C. Yan, H. Zhang, Z. Zhou, W. Yi, Identification of novel organo-Se BTSA-based derivatives as potent, reversible, and selective PPARγ covalent modulators for antidiabetic drug discovery, J. Med. Chem. (2024), https://doi.org/10.1021/ACS.JMEDCHEM.4C02803/SUPPL_FILE/JM4C02803_SI_002.CSV.
[14] F. Bril, D.M. Biernacki, S. Kalavalapalli, R. Lomonaco, S.K. Subbarayan, J. Lai, F. Tio, A. Suman, B.K. Orsak, J. Hecht, K. Cusi, Role of vitamin E for nonalcoholic steatohepatitis in patients with type 2 diabetes: a randomized controlled trial, Diabetes Care 42 (2019) 1481–1488, https://doi.org/10.2337/DC19-0167.
[15] S. Willems, L. Gellrich, A. Chaikuad, S. Kluge, O. Werz, J. Heering, S. Knapp, S. Lorkowski, M. Schubert-Zsilavecz, D. Merk, Endogenous vitamin E metabolites mediate allosteric PPARγ activation with unprecedented co-regulatory interactions, Cell Chem. Biol. 28 (2021) 1489–1500.e8, https://doi.org/10.1016/J.CHEMBIOL.2021.04.019.
[16] X. Zhang, F. Deng, Y. Zhang, X. Zhang, J. Chen, Y. Jiang, Pparγ attenuates hepatic inflammation and oxidative stress of non-alcoholic steatohepatitis via modulating the mir-21-5p/sfrp5 pathway, Mol. Med. Rep. 24 (2021) 1–11, https://doi.org/10.3892/MMR.2021.12463/HTML.
[17] J. Pan, W. Zhou, R. Xu, L. Xing, G. Ji, Y. Dang, Natural PPARs agonists for the treatment of nonalcoholic fatty liver disease, Biomed. Pharmacother. 151 (2022), https://doi.org/10.1016/J.BIOPHA.2022.113127.
[18] J. Chen, D. Liu, Q. Bai, J. Song, J. Guan, J. Gao, B. Liu, X. Ma, Y. Du, Celecoxib attenuates liver steatosis and inflammation in non-alcoholic steatohepatitis induced by high-fat diet in rats, Mol. Med. Rep. 4 (2011) 811–816, https://doi.org/10.3892/MMR.2011.501/HTML.
[19] F. Tian, Y.J. Zhang, Y. Li, Y. Xie, Celecoxib ameliorates non-alcoholic steatohepatitis in type 2 diabetic rats via suppression of the non-canonical Wnt signaling pathway expression, PLoS One 9 (2014), https://doi.org/10.1371/JOURNAL.PONE.0083819.
[20] G. Zhu, L. Chen, S. Liu, L. She, Y. Ding, C. Yang, F. Zhu, Celecoxib-mediated attenuation of non-alcoholic steatohepatitis is potentially relevant to redistributing the expression of adiponectin receptors in rats, Heliyon 8 (2022) e09872, https://doi.org/10.1016/J.HELIYON.2022.E09872.
[21] P. Puri, M.M. Wiest, O. Cheung, F. Mirshahi, C. Sargeant, H.K. Min, M.J. Contos, R. K. Sterling, M. Fuchs, H. Zhou, S.M. Watkins, A.J. Sanyal, The plasma lipidomic signature of nonalcoholic steatohepatitis, Hepatology 50 (2009) 1827–1838, https://doi.org/10.1002/HEP.23229.
[22] P.A. Elzahhar, R. Alaaeddine, T.M. Ibrahim, R. Nassra, A. Ismail, B.S.K. Chua, R. L. Frkic, J.B. Bruning, N. Wallner, T. Knape, A. von Knethen, H. Labib, A.F. El-Yazbi, A.S.F. Belal, Shooting three inflammatory targets with a single bullet: novel multi-targeting anti-inflammatory glitazones, Eur. J. Med. Chem. 167 (2019) 562–582, https://doi.org/10.1016/j.ejmech.2019.02.034.
[23] P.A. Elzahhar, R.A. Alaaeddine, R. Nassra, A. Ismail, H.F. Labib, M.G. Temraz, A.S. F. Belal, A.F. El-Yazbi, Challenging inflammatory process at molecular, cellular and in vivo levels via some new pyrazolyl thiazolones, J. Enzym. Inhib. Med. Chem. 36 (2021) 669–684, https://doi.org/10.1080/14756366.2021.1887169.
[24] M.A.W. Elkhatib, A. Mroueh, R.W. Rafeh, F. Sleiman, H. Fouad, E.I. Saad, M. A. Fouda, O. Elgaddar, K. Issa, A.H. Eid, A.A. Eid, K.S. Abd-Elrahman, A.F. El-Yazbi, Amelioration of perivascular adipose inflammation reverses vascular dysfunction in a model of nonobese prediabetic metabolic challenge: potential role of antidiabetic drugs, Transl. Res. 214 (2019) 121–143, https://doi.org/10.1016/J.TRSL.2019.07.009.
[25] N.M.Z. Bakkar, N. Mougharbil, A. Mroueh, A. Kaplan, A.H. Eid, S. Fares, F. A. Zouein, A.F. El-Yazbi, Worsening baroreflex sensitivity on progression to type 2 diabetes: localized vs. systemic inflammation and role of antidiabetic therapy, Am. J. Physiol. Endocrinol. Metab. 319 (2020) E835–E851, https://doi.org/10.1152/AJPENDO.00145.2020.
[26] C. Pirat, A. Farce, N. Lebègue, N. Renault, C. Furman, R. Millet, S. Yous, S. Speca, P. Berthelot, P. Desreumaux, P. Chavatte, Targeting peroxisome proliferator-activated receptors (PPARs): development of modulators, J. Med. Chem. 55 (2012) 4027–4061, https://doi.org/10.1021/jm101360s.
[27] H. Chen, H. Tan, J. Wan, Y. Zeng, J. Wang, H. Wang, X. Lu, PPAR-γ signaling in nonalcoholic fatty liver disease: pathogenesis and therapeutic targets, Pharmacol. Ther. 245 (2023), https://doi.org/10.1016/J.PHARMTHERA.2023.108391.
[28] L. Zhang, Y. Li, M. Chen, X. Su, D. Yi, P. Lu, D. Zhu, 15-LO/15-HETE mediated vascular adventitia fibrosis via p38 MAPK-dependent TGF-β, J. Cell. Physiol. 229 (2014) 245–257, https://doi.org/10.1002/JCP.24443.
[29] Y. Wen, J. Gu, S.K. Chakrabarti, K. Aylor, J. Marshall, Y. Takahashi, T. Yoshimoto, J.L. Nadler, The role of 12/15-lipoxygenase in the expression of interleukin-6 and tumor necrosis factor-alpha in macrophages, Endocrinology 148 (2007) 1313–1322, https://doi.org/10.1210/EN.2006-0665.
[30] H.S. Dwaib, A.F. El-Yazbi, Protocol for producing a rat model of non-obese prediabetes using a mild hypercaloric diet approach, STAR Protoc 5 (2024) 103276, https://doi.org/10.1016/J.XPRO.2024.103276.
[31] S.H. Hammoud, I. AlZaim, N. Mougharbil, S. Koubar, A.H. Eid, A.A. Eid, A.F. El-Yazbi, Peri-renal adipose inflammation contributes to renal dysfunction in a non-obese prediabetic rat model: role of anti-diabetic drugs, Biochem. Pharmacol. 186 (2021) 114491, https://doi.org/10.1016/j.bcp.2021.114491.
[32] S. Yasmin, F. Capone, A. Laghezza, F.D. Piaz, F. Loiodice, V. Vijayan, V. Devadasan, S.K. Mondal, Ö. Atll, M. Baysal, A.K. Pattnaik, V. Jayaprakash, A. Lavecchia, Novel benzylidene thiazolidinedione derivatives as partial PPARγ agonists and their antidiabetic effects on type 2 diabetes, Sci. Rep. 7 (1 7) (2017) 1–17, https://doi.org/10.1038/s41598-017-14776-0, 2017.
[33] P. Banerjee, E. Kemmler, M. Dunkel, R. Preissner, ProTox 3.0: a webserver for the prediction of toxicity of chemicals, Nucleic Acids Res. 52 (2024) W513–W520, https://doi.org/10.1093/NAR/GKAE303.
[34] S.I. Aboras, M.A. Korany, A.F. El-Yazbi, M.A.A. Ragab, H.H. Abdine, In-depth investigation of the Silymarin effect on the pharmacokinetic parameters of sofosbuvir, GS-331007 and ledipasvir in rat plasma using LC–MS, Biomed. Chromatogr. 36 (2022), https://doi.org/10.1002/bmc.5427.
[35] P. Macheras, Method of residuals: estimation of absorption and elimination rate constants having comparable values, Biopharm Drug Dispos. 8 (1987) 47–56, https://doi.org/10.1002/BDD.2510080106.
[36] H.H. Shaaban, I. Alzaim, A. El-Mallah, R.G. Aly, A.F. El-Yazbi, A. Wahid, Metformin, pioglitazone, dapagliflozin and their combinations ameliorate manifestations associated with NAFLD in rats via anti-inflammatory, anti-fibrotic, anti-oxidant and anti-apoptotic mechanisms, Life Sci. 308 (2022), https://doi.org/10.1016/J.LFS.2022.120956.
[37] A.J. Kroker, J.B. Bruning, Review of the structural and dynamic mechanisms of PPAR γ partial agonism, PPAR Res. 2015 (2015) 1–15, https://doi.org/10.1155/2015/816856.
[38] Y.M. Liao, L. Cheng, R.S. Luo, Q. Guo, W. Bin Shao, Y.M. Feng, X. Zhou, L.W. Liu, S. Yang, Discovery of new 1,2,4-triazole/1,3,4-oxadiazole-decorated quinolinones as agrochemical alternatives for controlling viral infection by inhibiting the viral replication and self-assembly process, J. Agric. Food Chem. (2024), https://doi.org/10.1021/ACS.JAFC.4C05234/SUPPL_FILE/JF4C05234_SI_001.PDF.
[39] E. Rajanarendar, S. Rama Krishna, D. Nagaraju, K. Govardhan Reddy, B. Kishore, Y. N. Reddy, Environmentally benign synthesis, molecular properties prediction and anti-inflammatory activity of novel isoxazolo[5,4-d]isoxazol-3-yl-aryl-methanones via vinylogous Henry nitroaldol adducts as synthons, Bioorg. Med. Chem. Lett 25 (2015) 1630–1634, https://doi.org/10.1016/J.BMCL.2015.01.041.
[40] H.W. Liu, S.S. Su, S.Y. Ma, T. Li, W. Fang, Y. Ding, S.T. Liu, J.R. Zhang, H.M. Xiang, X. Zhou, S. Yang, Discovery and structural optimization of 1,2,3,4-Tetrahydro-β-carbolines as novel reactive oxygen species inducers for controlling intractable plant bacterial diseases, J. Agric. Food Chem. 71 (2023) 11035–11047, https://doi.org/10.1021/ACS.JAFC.3C02615/SUPPL_FILE/JF3C02615_SI_001.PDF.
[41] Y. Yang, S. Ma, T. Li, J. He, S. Liu, H. Liu, J. Zhang, X. Zhou, L. Liu, S. Yang, Discovery of novel ursolic acid derivatives as effective antimicrobial agents through a ROS-mediated apoptosis mechanism, Front. Chem. Sci. Eng. 17 (12 17) (2023) 2101–2113, https://doi.org/10.1007/S11705-023-2361-5, 2023.
[42] D.F. Veber, S.R. Johnson, H.-Y. Cheng, B.R. Smith, K.W. Ward, K.D. Kopple, Molecular properties that influence the oral bioavailability of drug candidates, J. Med. Chem. 45 (2002) 2615–2623, https://doi.org/10.1021/jm020017n.
[43] M.E. Kavanagh, M.R. Doddareddy, M. Kassiou, The development of CNS-active LRRK2 inhibitors using property-directed optimisation, Bioorg. Med. Chem. Lett 23 (2013) 3690–3696, https://doi.org/10.1016/j.bmcl.2013.04.086.
[44] C. Abad-Zapatero, Ligand efficiency indices for effective drug discovery, Expet Opin. Drug Discov. 2 (2007) 469–488, https://doi.org/10.1517/17460441.2.4.469.
[45] A.L. Hopkins, C.R. Groom, A. Alex, Ligand efficiency: a useful metric for lead selection, Drug Discov. Today 9 (2004) 430–431, https://doi.org/10.1016/S1359-6446(04)03069-7.
[46] A.L. Hopkins, G.M. Keserü, P.D. Leeson, D.C. Rees, C.H. Reynolds, The role of ligand efficiency metrics in drug discovery, Nat. Rev. Drug Discov. 13 (2014) 105–121, https://doi.org/10.1038/nrd4163.
[47] H.H. Kinfe, Y.H. Belay, Synthesis and biological evaluation of novel thiosemicarbazone – triazole hybrid compounds antimalarial agents, S. Afr. J. Chem. 66 (2013) 130–135.
[48] B. Negi, D. Kumar, W. Kumbukgolla, S. Jayaweera, P. Ponnan, R. Singh, S. Agarwal, D.S. Rawat, Anti-methicillin resistant Staphylococcus aureus activity, synergism with oxacillin and molecular docking studies of metronidazole-triazole hybrids, Eur. J. Med. Chem. 115 (2016) 426–437, https://doi.org/10.1016/J.EJMECH.2016.03.041.
[49] T.H. Sum, T.J. Sum, W.R.J.D. Galloway, S. Collins, D.G. Twigg, F. Hollfelder, D. R. Spring, Combinatorial synthesis of structurally diverse triazole-bridged flavonoid dimers and trimers, Molecules 21 (2016) 1230, https://doi.org/10.3390/MOLECULES21091230, 21 (2016) 1230.
[50] M.G. Temraz, P.A. Elzahhar, A. El-Din, A. Bekhit, A.A. Bekhit, H.F. Labib, A.S. F. Belal, Anti-leishmanial click modifiable thiosemicarbazones: design, synthesis, biological evaluation and in silico studies, Eur. J. Med. Chem. 151 (2018) 585–600, https://doi.org/10.1016/j.ejmech.2018.04.003.
[51] A. Nagarsenkar, L. Guntuku, S.D. Guggilapu, D.B. K, S. Gannoju, V.G.M. Naidu, N. B. Bathini, Synthesis and apoptosis inducing studies of triazole linked 3-benzylidene isatin derivatives, Eur. J. Med. Chem. 124 (2016) 782–793, https://doi.org/10.1016/j.ejmech.2016.09.009.
[52] P.A. Elzahhar, S.M. Abd El Wahab, M. Elagawany, H. Daabees, A.S.F. Belal, A.F. El-Yazbi, A.H. Eid, R. Alaaeddine, R.R. Hegazy, R.M. Allam, M.W. Helmy, Bahaa Elgendy, A. Angeli, S.A. El-Hawash, C.T. Supuran, BahaaElgendy, A. Angeli, S.A. El-Hawash, C.T. Supuran, Expanding the anticancer potential of 1,2,3-triazoles via simultaneously targeting Cyclooxygenase-2, 15-lipoxygenase and tumor-associated carbonic anhydrases, Eur. J. Med. Chem. 200 (2020) 112439, https://doi.org/10.1016/j.ejmech.2020.112439.
[53] B.R.P. Kumar, M. Soni, S.S. Kumar, K. Singh, M. Patil, R.B.N. Baig, L. Adhikary, Synthesis, glucose uptake activity and structure-activity relationships of some novel glitazones incorporated with glycine, aromatic and alicyclic amine moieties via two carbon acyl linker, Eur. J. Med. Chem. 46 (2011) 835–844, https://doi.org/10.1016/j.ejmech.2010.12.019.

[54] K. Kar, U. Krithika, Mithuna, P. Basu, S. Santhosh Kumar, A. Reji, B.R. Prashantha Kumar, Design, synthesis and glucose uptake activity of some novel glitazones, Bioorg. Chem. 56 (2014) 27–33, https://doi.org/10.1016/j.bioorg.2014.05.006.
[55] X. Liu, S. Ouyang, B. Yu, Y. Liu, K. Huang, J. Gong, S. Zheng, Z. Li, H. Li, H. Jiang, PharmMapper server: a web server for potential drug target identification using pharmacophore mapping approach, Nucleic Acids Res. 38 (2010) W609–W614, https://doi.org/10.1093/NAR/GKQ300.
[56] D.A. Filimonov, A.A. Lagunin, T.A. Gloriozova, A.V. Rudik, D.S. Druzhilovskii, P. V. Pogodin, V.V. Poroikov, Prediction of the biological activity spectra of organic compounds using the pass online web resource, Chem. Heterocycl. Compd. 50 (2014) 444–457, https://doi.org/10.1007/S10593-014-1496-1/FIGURES/4.
[57] S.X. Ge, D. Jung, D. Jung, R. Yao, ShinyGO: a graphical gene-set enrichment tool for animals and plants, Bioinformatics 36 (2020) 2628–2629, https://doi.org/10.1093/BIOINFORMATICS/BTZ931.
[58] S. Arifi, J.A. Marschner, J. Pollinger, L. Isigkeit, P. Heitel, A. Kaiser, L. Obeser, G. Höfner, E. Proschak, S. Knapp, A. Chaikuad, J. Heering, D. Merk, Targeting the alternative vitamin E metabolite binding site enables noncanonical PPARγ modulation, J. Am. Chem. Soc. 145 (2023) 14802–14810, https://doi.org/10.1021/JACS.3C03417/SUPPL_FILE/JA3C03417_SI_003.ZIP.
[59] P.A. Elzahhar, R. Orioli, N.W. Hassan, S. Gobbi, F. Belluti, H.F. Labib, A.F. El-Yazbi, R. Nassra, A.S.F. Belal, A. Bisi, Chromone-based small molecules for multistep shutdown of arachidonate pathway: simultaneous inhibition of COX-2, 15-LOX and mPGES-1 enzymes, Eur. J. Med. Chem. 266 (2024), https://doi.org/10.1016/J.EJMECH.2024.116138.
[60] Y.H. Han, D.Q. Chen, M.H. Jin, Y.H. Jin, J. Li, G.N. Shen, W.L. Li, Y.X. Gong, Y. Y. Mao, D.P. Xie, D.S. Lee, L.Y. Yu, S.U. Kim, J.S. Kim, T. Kwon, Y.D. Cui, H.N. Sun, Anti-inflammatory effect of hispidin on LPS induced macrophage inflammation through MAPK and JAK1/STAT3 signaling pathways, Appl Biol Chem 63 (2020) 1–9, https://doi.org/10.1186/S13765-020-00504-2/FIGURES/4.
[61] M.J. Naim, M.J. Alam, F. Nawaz, V.G.M. Naidu, S. Aaghaz, M. Sahu, N. Siddiqui, O. Alam, Synthesis, molecular docking and anti-diabetic evaluation of 2,4-thiazolidinedione based amide derivatives, Bioorg. Chem. 73 (2017) 24–36, https://doi.org/10.1016/J.BIOORG.2017.05.007.
[62] N.W. Hassan, A. Sabt, M.A.Z. El-Attar, M. Ora, A.E.D.A. Bekhit, K. Amagase, A. A. Bekhit, A.S.F. Belal, P.A. Elzahhar, Modulating leishmanial pteridine metabolism machinery via some new coumarin-1,2,3-triazoles: design, synthesis and computational studies, Eur. J. Med. Chem. 253 (2023) 115333, https://doi.org/10.1016/J.EJMECH.2023.115333.
[63] A. Daina, O. Michielin, V. Zoete, SwissADME: a free web tool to evaluate pharmacokinetics, drug-likeness and medicinal chemistry friendliness of small molecules, Sci. Rep. 7 (1 7) (2017) 1–13, https://doi.org/10.1038/srep42717, 2017.